J. Phys.: Condens. Matter **21** (2009) 104208 (17pp) doi:10.1088/0953-8984/21/10/104208

Multiplet calculations of $L_{2,3}$ x-ray absorption near-edge structures for 3d transition-metal compounds

Hidekazu Ikeno[1], Frank M F de Groot[2], Eli Stavitski[2] and Isao Tanaka[1,3]

[1] Department of Materials Science and Engineering, Kyoto University, Yoshida, Sakyo, Kyoto 606-8501, Japan
[2] Department of Inorganic Chemistry and Catalysis, Utrecht University, Sorbonnelaan 16, 3584 CA Utrecht, The Netherlands
[3] Nanostructures Research Laboratory, Japan Fine Ceramics Center, Atsuta, Nagoya 456-8587, Japan

E-mail: ikeno@t02.mbox.media.kyoto-u.ac.jp

Received 14 October 2008, in final form 12 December 2008
Published 10 February 2009
Online at stacks.iop.org/JPhysCM/21/104208

Abstract
The purpose of this work is to compare the two different procedures to calculate the $L_{2,3}$ x-ray absorption spectra of transition-metal compounds: (1) the semi-empirical charge transfer multiplet (CTM) approach and (2) the *ab initio* configuration-interaction (CI) method based on molecular orbitals. We mainly focused on the difference in the treatment of ligand field effects and the charge transfer effects in the two methods. The reduction of multiplet interactions due to the solid state effects has been found by the *ab initio* CI approach. We have also found that the mixing between the original and the charge transferred configurations obtained by the *ab initio* CI approach is smaller than that obtained by the CTM approach, since charge transfer through the covalent bonding between metal and ligand atoms has been included by taking the molecular orbitals as the basis functions.

(Some figures in this article are in colour only in the electronic version)

1. Introduction

The $L_{2,3}$ x-ray absorption spectra relate to the transition of a 2p core state to an empty state. At the edge, the spectra are dominated by the 2p3d transitions. This paper discusses two routes to calculate the $L_{2,3}$ x-ray absorption near-edge structures for 3d transition-metal compounds.

(a) The charge transfer multiplet (CTM) approach.
(b) The *ab initio* configuration-interaction (*ab initio* CI) approach based on molecular orbitals.

The foremost motivation for writing this paper is the comparison of the semi-empirical CTM approach and the route towards a more *ab initio* approach, which is an important motive for the development of the *ab initio* CI method. We first introduce the CTM approach in section 2. Sections 3 and 4 then compare the *ab initio* CI approach. Section 5 compares both multiplet models to other procedures to simulate the $L_{2,3}$ x-ray absorption spectra.

2. The charge transfer multiplet approach

Below, we discuss the main aspects of the charge transfer multiplet (CTM) approach. A more detailed discussion is given in the recent book on the core level spectroscopy of solids [1].

2.1. Atomic multiplet effects

The metal 2p core electrons are excited with the dipole transition into the 3d and 4s valence states. The transition matrix elements to the 4s states are negligible and one mainly observes the 2p3d transitions. Because of the strong 2p3d wavefunction overlap, or more precisely the intra-atomic 2p3d two-electron integrals, the x-ray absorption spectrum (XAS) is

strongly modified from the empty 3d density of states: this is the multiplet effect [2, 3].

In the final state of the 2p XAS process, a partly filled $2p^5$ core state interacts with a partly filled 3d band. For example, the Ni^{2+} ions in NiO can be approximated as a $3d^9$ configuration. The 2p hole and the 3d electron have radial wavefunctions that overlap significantly. This wavefunction overlap is an atomic effect that can be very large. It creates final states that are found after the vector coupling of the 2p and 3d wavefunctions. This effect is well known in atomic physics and actually plays a crucial role in the calculation of atomic spectra [4]. Experimentally it was shown that, while the direct core hole potential is largely screened, these so-called multiplet effects are hardly screened in the solid state. This implies that the atomic multiplet effects are of the same order of magnitude in atoms and in solids. In the charge transfer multiplet approach one usually assumes that the solid state has the same Slater integral values as the free atom. Because the Slater integrals are usually calculated with the Hartree–Fock approach within the `RCN` code of Cowan, these HF values are reduced by 20% to take into account configuration-interaction (CI) effects. These 80% of HF values describe the atomic spectra well [4].

Atomic multiplet effects have been described in detail elsewhere [1, 5]. Here we briefly introduce some concepts. The number of peaks in an L-edge atomic multiplet spectrum is limited and also the calculation is very small in size. As has been shown in detail in the core level spectroscopy of solids, the calculation of $3d^0$ systems ($3d^0 \rightarrow 2p^5 3d^1$) implies a single initial state and a 3×3 matrix for the $J = 1$ final states. The largest matrix for a $3d^n$ ground state is found for $n = 5$ with ${}_{10}C_5$ is 252 states, where this matrix can be separated into different J values with the largest matrix for the $J = 5/2$ state with 10 states. The largest final state matrix has six times 252, or 1512 states. For the $3d^5 \rightarrow 2p^5 3d^6$ transition, the ground state has $J = 5/2$ and the three allowed final states (with a selection rule $\Delta J = 0, \pm 1$) have respectively 35, 39 and 36 states for $J = 3/2, 5/2$ and $7/2$. The largest final state diagonalization is for a 39×39 matrix and the largest calculation for the transition matrix element is 10×39. These are very small matrices for present-day computer power and hence these calculations only take a fraction of a second.

2.2. Crystal field effects

The crystal field model approximates the transition metal as an isolated atom surrounded by a distribution of charges that should mimic the actual solid. It turned out that such a crystal field model could explain a large range of experiments, including optical spectra, electron paramagnetic resonance (EPR) spectra and x-ray absorption spectra. An important reason for the success of the crystal field model is that the explained properties are mainly determined by symmetry considerations. The crystal field model makes use of group theory, and in group theory terminology the only thing crystal field theory does is to transfer the spectra obtained in atomic symmetry to cubic symmetry and subsequently to any other point group. Details of the crystal field multiplet approach for L-edge spectra are given elsewhere [2, 3, 5].

Here we extend the discussion on the matrix sizes that play a role in crystal field theory. The $3d^0 \rightarrow 2p^5 3d^1$ transition was a 1×3 calculation, where the largest matrix was the 3×3 final state. In cubic symmetry, this calculation transfers to a 1×7 transition calculation, due to the admixture of more symmetry states via the crystal field Hamiltonian. The largest $3d^5 \rightarrow 2p^5 3d^6$ transition was a 10×39 calculation. In cubic symmetry, this calculation transfers to a number of transitions for the different symmetries in cubic symmetry, the largest of which is a 42×210 transition calculation. These numbers remain small and all crystal field multiplet calculations run in only a few seconds.

2.3. Charge transfer effects

Charge transfer effects are the effects of charge fluctuations in the initial and the final states, which can be described by the combination of different ground state and final state configurations. In the case of transition-metal oxides, the most important charge transfer channel is the transition of a $3d^N$ configuration to a $3d^{N+1}\underline{L}$ configuration, where a ligand electron is transferred to the metal site and a ligand hole $\underline{L}$ is created. In principle, this is a combination of a $3d^{N+1}$ site and a ligand hole site at infinite distance. This charge transfer channel is one of the two main channels discussed in the Zaanen–Sawatzky–Allen model of the electronic structure of transition-metal systems [6]. The other important channel is the metal–metal charge transfer, where a $3d^N 3d^N$ configuration is modified into a $3d^{N+1}3d^{N-1}$ configuration. To include such a channel explicitly, at least two metal ions must be included in the calculation, which is not the case in the charge transfer multiplet (CTM) model.

The main reason that L edges (in contrast to 2p x-ray photoemission) can be described well without the including of charge transfer is that the creation of a 2p core hole transfers the extra electron to the 3d band, which is essentially a charge conserving optical transition. This implies that the ordering of states remains similar to the ground state, where it is noticed that each $3d^N$ configuration consists of the full crystal field multiplet manifold.

In the CTM model, the ligand hole state is described as a delocalized d wavefunction that is described without correlation effects within itself and without correlation effects with other states. This approach mimics the description of the actual p orbitals of the ligand states and the delocalized d wavefunction can be envisaged as a combined wavefunction of the ligand states. Because the delocalized d wavefunction has one hole, its dimension is 10. The largest calculation for two configurations is the $3d^4 + 3d^5\underline{L} \rightarrow 2p^5 3d^5 + 2p^5 3d^6\underline{L}$ calculation that in C_4 symmetry includes matrix sizes up to 3150. Because of the use of approximated diagonalization routines, the calculation time is approximately 10 min on a regular PC or laptop.

In addition to the addition of a $3d^{N+1}\underline{L}$ configuration to a $3d^N$ ground state, the CTM program has the option to include more configurations, for example adding the next charge transfer state $3d^{N+2}\underline{L}^2$, adding the metal–ligand charge transfer $3d^{N-1}L$, adding two different charge transfer channels

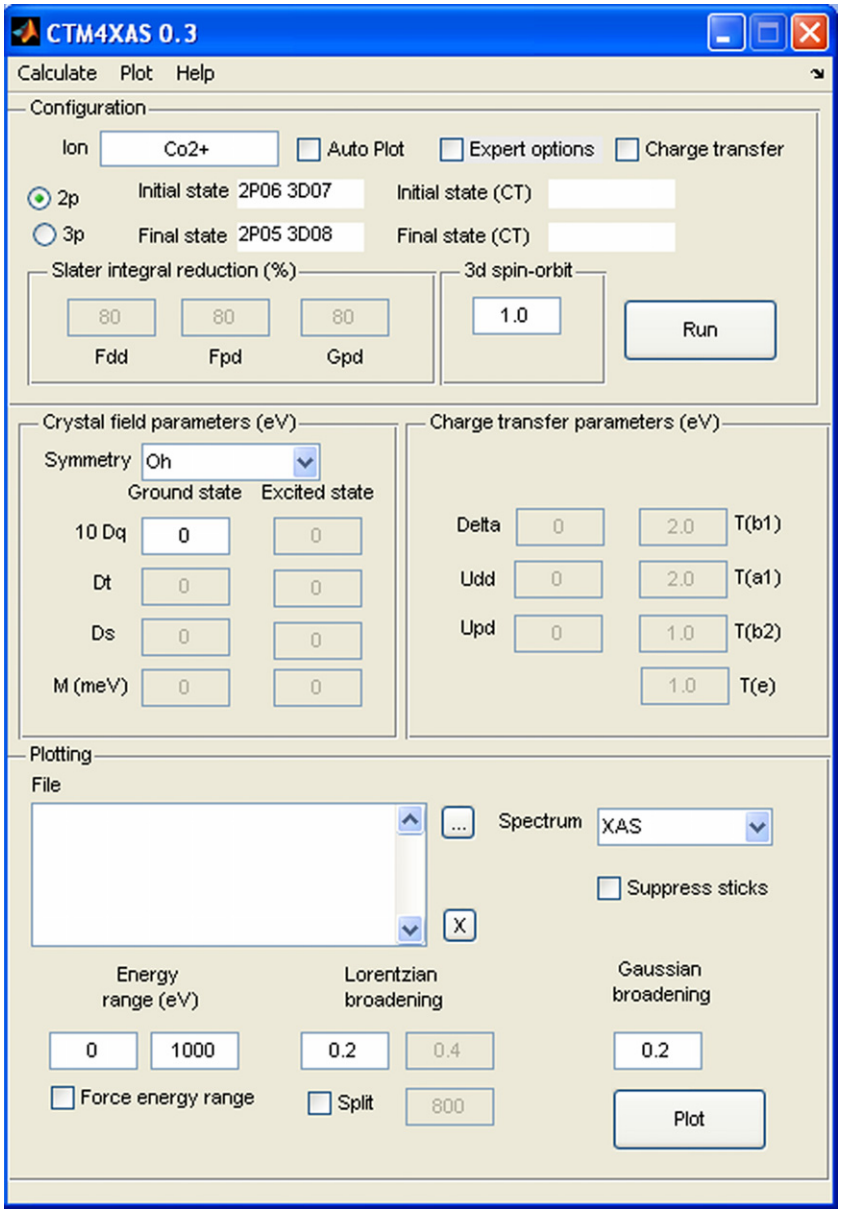

Figure 1. The layout of the CTM4XAS graphical user interface for the charge transfer multiplet programs.

$3d^{N+1}\underline{L}^a$ and $3d^{N+1}\underline{L}^b$, where $\underline{L}^a$ and $\underline{L}^b$ are related to two different ligand bands at different excitation energies and coupling strengths [7].

Description of systems with strong π-bonds. In systems that contain significant ligand metal charge transfer (LMCT) as well as metal ligand charge transfer (MLCT), this has to be included explicitly. This implies the inclusion of three configurations $3d^N + 3d^{N+1}\underline{L} + 3d^{N-1}L$. The $3d^{N+1}\underline{L}$ configuration takes care of the ligand metal charge transfer and $3d^{N-1}L$ relates to metal ligand charge transfer effects, including π-back bonding. This method turned out to describe well systems with strong π-bonds, for example iron cyanides [8] and iron-heme systems [9]. An interesting approach to correlate CTM analysis with *ab initio* density functional theory (DFT) calculations was developed by Wasinger *et al* [10]. They performed detailed spectral fits of a series of iron complexes, using the charge transfer multiplet approach. In addition, they performed DFT calculations of the ground states, using the ADF code. They analyzed the distribution of the 3d band into metal 3d character and oxygen character and compared the DFT results to a analysis of the ground states as used in the optimized charge transfer multiplet simulations. An excellent correlation between DFT and CTM was found for the electron distribution over the 3d orbitals.

2.4. Calculations with the CTM4XAS *graphical user interface*

The charge transfer multiplet calculations as described above have recently been included in the CTM4XAS user interface. Figure 1 shows the layout of the interface. The input is divided into four panels, respectively the atomic parameters (top), the crystal field parameters (left, middle), the charge

transfer parameters (right, middle) and the plotting options (bottom). As yet, CTM4XAS provides the 2p and 3p XAS spectra plus their XMCD spectra. The program is freely available from the authors. Future versions of CTM4XAS will include the calculation of x-ray photoemission (XPS), resonant photoemission and Auger spectra plus x-ray emission and resonant x-ray emission spectra.

2.5. Parameters as used in the CTM4XAS *simulations*

The CTM4XAS simulations use a number of semi-empirical parameters. For a transition-metal ion in octahedral symmetry, the crystal field multiplet calculation uses an empirical value of the crystal field splitting 10 Dq. This can be derived from other experiments, for example optical absorption or EPR. Alternatively, it could be calculated, for example, from a DFT-based calculation, similar to the DFT calculations that are used for the *ab initio* CI calculations as discussed below.

The charge transfer multiplet calculations use a number of additional parameters: the charge transfer energy Δ, the Hubbard U_{3d3d} and the core hole potential U_{2p3d}. The charge transfer energy and the Hubbard U can be derived from trends in the 3d series or from additional experiments, in particular XPS. The core hole potential U_{2p3d} or Q is assumed to be 1–2 eV larger than U. In addition, the hopping parameters T have to be determined. They can be calculated from a tight-binding fit to DFT calculations [1].

3. *Ab initio* multiplet approach

The charge transfer multiplet method is the most prevalent and conventional theoretical approach for the analysis of TM-$L_{2,3}$ XANES. Although this approach has been successful in reproducing many experimental spectra, it cannot be used to predict multiplet structure *a priori*, because of the use of the adjustable parameters. An *ab initio* calculation that takes multiplet effects into account is therefore strongly desirable.

For this purpose, the Tanaka group in Kyoto has developed a relativistic configuration-interaction program in quantum chemistry. The molecular orbitals (MOs) obtained by relativistic density functional theory (DFT) were used as basis functions for the CI calculations. In this paper, we simply call this method the '*ab initio* CI' method. Experimental spectra from many compounds having different d-electron numbers and coordination numbers have been successfully reproduced without empirical parameters [11–13]. In this section, the theoretical background of the *ab initio* CI method is described in detail.

3.1. Dirac equation and its non-relativistic limit

The wave equation for an electron, consistent with both the principles of quantum mechanics and the theory of special relativity, was formulated by Paul Dirac (see chapter XI of [14]). The Dirac equation of a spin-1/2 particle in the potential, $v(\boldsymbol{r})$, which does not explicitly depend on time, is given by

$$\hat{h}_{\mathrm{D}}\phi = \epsilon\phi, \tag{1}$$

$$\hat{h}_{\mathrm{D}} = c\boldsymbol{\alpha}\cdot\boldsymbol{p} + mc^2\beta + v(\boldsymbol{r}). \tag{2}$$

where c is the velocity of light, and $\boldsymbol{\alpha}$ and β are 4×4 Dirac matrices acting on the one-electron wavefunction. The Dirac matrices were obtained so that the square of the energy of a free particle, $E_0 = c\boldsymbol{\alpha}\cdot\boldsymbol{p} + mc^2$, should satisfy the relation among the energy, the momentum and the rest mass in special relativity, $E_0^2 = c^2|\boldsymbol{p}|^2 + m^2c^4$. Since the Dirac Hamiltonian holds 4×4 matrices, the eigenfunction ϕ must be a four-component vector. Thus a fully relativistic wavefunction contains the four degrees of freedom: two of them are associated with the group of eigenstates with positive and negative energy, and each group holds two degrees of freedom corresponding to the probability amplitude for up-spin and down-spin along with a specified direction. The positive energy state, which is dominated by the first and the second component, describes an electronic state, while the negative energy state, dominated by the third and the fourth component, describes a positronic state.

The most important relativistic effect for the TM-$L_{2,3}$ XANES is the spin–orbit coupling. In the CTM approach, the spin–orbit coupling is usually treated as the correction term to the non-relativistic Schrödinger equation. The analytic form of the spin–orbit coupling term can be derived from the Dirac equation by eliminating the minor components (the third and the fourth components) of the wavefunction from (1) and considering the non-relativistic limit where c is much larger compared with the velocity of electrons [15]. Thus, the spin–orbit coupling and other relativistic effects are automatically included by solving the Dirac equation.

3.2. Relativistic many-electron Hamiltonian

In order to calculate TM-$L_{2,3}$ XANES for atoms, molecules and solids, we have to consider the motion of the multiple interacting electrons with the electrostatic potential from the nuclei. Quantum electrodynamics (QED), which is the relativistic quantum field theory, is the most accurate theory in physics to describe the interactions of electrons [16]. QED describes the motion of electrons and positrons (antiparticles of electrons) interacting with each other by the exchange of photons. In general, the Hamiltonian of QED only conserves the total charge in the system, but not the number of particles, since virtual photons can be transformed into virtual electron–positron pairs. For the calculation of atoms, molecules and solids, an approximated Hamiltonian which refers to N electrons without any positrons and photons is commonly used. This approach is known as the 'no-pair' approximation [17–19]. The approximated 'no-pair' Hamiltonian is expressed as

$$\hat{H}_{\mathrm{np}} = \sum_{i=1}^{N}\hat{h}(\boldsymbol{r}_i) + \tfrac{1}{2}\sum_{i=1,\ j\neq i}^{N}\Lambda_+\hat{g}(\boldsymbol{r}_i,\boldsymbol{r}_j)\Lambda_+. \tag{3}$$

Here, the operator Λ_+ is defined as the product $\Lambda_+(1)\Lambda_+(2)\cdots\Lambda_+(N)$, with $\Lambda_+(i)$ the projection operator onto the space spanned by the positive eigenstates (electronic states) of some one-electron Hamiltonian. By using the projection operator

Λ_+, virtual electron–photon pairs are eliminated from the Hamiltonian. $h(\boldsymbol{r}_i)$ is a one-particle Dirac operator given by

$$\hat{h}(\boldsymbol{r}_i) = c\boldsymbol{\alpha}_i \cdot \boldsymbol{p}_i + mc^2\beta_i + v_{\mathrm{nuc}}(\boldsymbol{r}_i) + v_{\mathrm{ext}}(\boldsymbol{r}_i), \qquad (4)$$

where $v_{\mathrm{nuc}}(\boldsymbol{r}_i)$ is the electrostatic potential from nuclei and $v_{\mathrm{ext}}(\boldsymbol{r}_i)$ is an external static potential such as the Madelung potential. $\hat{g}(\boldsymbol{r}_i, \boldsymbol{r}_j)$ is a two-electron operator which describes inter-electron interactions. We have adopted the instantaneous Coulomb interaction operator:

$$\hat{g}(\boldsymbol{r}_i, \boldsymbol{r}_j) = \frac{1}{4\pi\epsilon_0}\frac{e^2}{|\boldsymbol{r}_i - \boldsymbol{r}_j|} \qquad (5)$$

as a non-relativistic case. In this case, the Hamiltonian (3) is called the 'no-pair' Dirac–Coulomb Hamiltonian. Though the relativistic effects on inter-electron interactions are neglected, the 'no-pair' Dirac–Coulomb Hamiltonian is expected to be a good approximation for the $L_{2,3}$ XANES of 3d TM compounds. The influences of relativistic correction terms in QED for the Coulomb interactions were discussed elsewhere [20].

3.3. Relativistic configuration-interaction method

Using the relativistic 'no-pair' formalism, almost all methods in quantum chemistry formulate the non-relativistic many-electron problem, such as the Hartree–Fock method, the configuration-interaction method (CI), the coupled-cluster method (CC), the multi-configuration self-consistent-field method (MCSCF) and the many-body perturbation theory (MBPT), can be extended for the relativistic problem in a straightforward manner [21–28].

In this section, the CI method is explained in detail. The CI method is a post-self-consistent field (SCF) method to solve the non-relativistic (Schrödinger) equation or the relativistic equation for many-electron systems. In quantum chemistry, the CI method is mainly used to improve the ground state wavefunction by including the electronic correlation effects. The CI method is also useful for spectroscopy since it can explicitly calculate many-electron eigenstates corresponding to both ground and excited states and it is convenient to calculate transition probabilities of spectra.

In order to obtain the approximate eigenfunctions and eigenvalues of $\hat{H}_{\mathrm{np}}$, one chooses a finite orthonormal basis set of one-particle states at first. In practice, the electronic eigenstates $\{\phi_i | i = 1, 2, \ldots, L\}$ $(N < L)$ of the one-particle Dirac operator:

$$\hat{h}'(\boldsymbol{r}) = \hat{h}(\boldsymbol{r}) + U_{\mathrm{eff}}(\boldsymbol{r}), \qquad (6)$$

are used as a basis set, where $U_{\mathrm{eff}}(\boldsymbol{r})$ is an approximated potential of inter-electron interactions. In most cases, the Dirac–Hartree–Fock method, the relativistic version of the Hartree–Fock method, is used to calculate $\{\phi_i\}$. In the Dirac–Hartree–Fock method, the electronic correlation effects are not included in the equation: these effects are taken into account through CI. The alternative choice is using the solutions of the Dirac–Kohn–Sham equation, which is the one-particle Dirac equation derived from the relativistic density functional theory [29–31]. In the Dirac–Kohn–Sham equation, the electron correlation effects are approximately included through the exchange–correlation potential whose exact formalism is not known. Therefore, the correction of the electronic correlation effects are taken into account through CI based on Dirac–Kohn–Sham orbitals.

Once one-electron states $\{\phi_i \mid i = 1, 2, \ldots, L\}$ are obtained, the 'no-pair' Hamiltonian can be expressed in the second quantized form as

$$\hat{H} = \sum_{i,j=1}^{L} \langle i|\hat{h}|j\rangle a_i^\dagger a_j + \tfrac{1}{2}\sum_{i,j,k,l=1}^{L} \langle ij|\hat{g}|kl\rangle a_i^\dagger a_j^\dagger a_l a_k, \qquad (7)$$

where $\langle i|\hat{h}|j\rangle$ and $\langle ij|\hat{g}|kl\rangle$ are, respectively, the one-electron and the two-electron integrals defined as

$$\langle i|\hat{h}|j\rangle = \int \phi_i^*(\boldsymbol{r})\hat{h}(\boldsymbol{r})\phi_j(\boldsymbol{r})\,\mathrm{d}\boldsymbol{r}, \qquad (8)$$

$$\langle ij|\hat{g}|kl\rangle = \iint \phi_i^*(\boldsymbol{r}_1)\phi_j^*(\boldsymbol{r}_2)\hat{g}(\boldsymbol{r}_1, \boldsymbol{r}_2)\phi_k(\boldsymbol{r}_1)\phi_l(\boldsymbol{r}_2)\,\mathrm{d}\boldsymbol{r}_1\,\mathrm{d}\boldsymbol{r}_2. \qquad (9)$$

a_i and $a_i^\dagger$ denote the creation and annihilation operator for an electron in the one-electron state ϕ_i, respectively, which satisfy the following anti-commutation relations:

$$\begin{aligned} \{a_i, a_j\} = \{a_i^\dagger, a_j^\dagger\} = 0, \\ \{a_i, a_j^\dagger\} = \delta_{ij}. \end{aligned} \qquad (10)$$

The N-electron wavefunctions can be expressed as a linear combination of N-electron Slater determinants constructed from L orthonormal one-electron functions $\{\phi_i\}$:

$$|\Psi_k\rangle = \sum_p C_{pk}|\Phi_p\rangle. \qquad (11)$$

Here, $|\Phi_p\rangle = a_{p_1}^\dagger \cdots a_{p_N}^\dagger|\mathrm{vac}\rangle$ are the Slater determinants constructed from $p_1, \ldots, p_N$ th one-electron states, where $|\mathrm{vac}\rangle$ is the vacuum state, and the sum in (11) runs over all possible N combinations from L indexes of one-electron states. The coefficients C_{pk} in (11) for the 'no-pair' Dirac–Coulomb Hamiltonian $\hat{H}$ can be determined by using the standard Rayleigh–Ritz variational method. The Hamiltonian matrix elements are evaluated as

$$\begin{aligned} \langle\Phi_p|\hat{H}|\Phi_q\rangle = &\sum_{i,j=1}^{L} \langle i|\hat{h}|j\rangle\langle\Phi_p|a_i^\dagger a_j|\Phi_q\rangle \\ &+ \tfrac{1}{2}\sum_{i,j,k,l=1}^{L} \langle ij|\hat{g}|kl\rangle\langle\Phi_p|a_i^\dagger a_j^\dagger a_l a_k|\Phi_q\rangle. \end{aligned} \qquad (12)$$

Then the coefficient C_{pk} is obtained by diagonalizing this Hamiltonian matrix as the eigenvectors with the corresponding eigenvalues.

In principle, we can determine the ${}_LC_N$ number of coefficients C_{pk} in (11). In quantum chemistry, this method is called the 'full-CI', whose solutions give the best description of many-electron states for a given finite basis set $\{\phi_i | i = 1, 2, \ldots, L\}$. However, the full-CI is only possible if both the number of electrons N and the basis size L are

small. Otherwise the number ${}_LC_N$ of Slater determinants and corresponding coefficients becomes too large to compute. It is possible to significantly reduce this number by using the symmetry of the system, but the remaining numbers are still enormously large. Therefore the full-CI method is only applicable to the very limited system, and in practice, CI calculations are carried out with restricted electronic configurations to reduce the number of variational parameters, C_{pk}.

3.4. DFT–CI

Further reduction of computational costs is achieved by taking the hybrid method of density functional theory (DFT) and the CI method. In this approach, electronic correlations among particularly important orbitals are taken into account by the CI scheme, while correlations among other orbitals are approximately treated within the framework of DFT [11, 32]. We call this method the 'DFT–CI' method. The effective 'no-pair' Hamiltonian for selected M orbitals ($M < L$) can be described as

$$\hat{H}_{\rm eff} = \sum_{i,j=1}^{M} \langle i|\hat{h} + U'_{\rm eff}|j\rangle a_i^\dagger a_j + \tfrac{1}{2}\sum_{i,j,k,l=1}^{M} \langle ij|\hat{g}|kl\rangle a_i^\dagger a_j^\dagger a_l a_k. \quad (13)$$

Here $U'_{\rm eff}(\boldsymbol{r}_i)$ denotes the approximated exchange correlation potential from the electrons occupying the $L - M$ orbitals treated with DFT. The Hamiltonian matrix elements are evaluated using (12), which sums only over the selected M orbitals. Therefore we only need to calculate the one- and two-electron integrals, (8) and (9), among selected M orbitals. It helps to reduce the computational time, especially for the evaluation of the two-electron integrals, as the number of two-electron integrals is of the order of $O(M^4)$. However, the quality of eigenstates obtained depends on the exchange–correlation potentials used in the calculations. Such potential dependence can be reduced by taking an increasing number of selected orbitals M.

3.5. Photo-absorption cross section

X-ray absorption spectroscopy measures the x-ray absorption coefficient, μ, depending on the photon energy $E = \hbar\omega$. μ is proportional to the photo-absorption cross section (PACS), $\sigma_{\rm abs}$, of a single atom. According to 'Fermi's Golden Rule', $\sigma_{\rm abs}(E)$ of an N-electron atom for x-rays polarized in the $\boldsymbol{\epsilon}$ direction and with the wavenumber $\boldsymbol{k}$ is given by

$$\sigma_{\rm abs}(E) = \sum_{\rm f} \frac{4\pi^2\hbar^2\alpha}{m^2 E} \left|\left\langle \Psi_{\rm f}\left|\sum_{j=1}^{N} {\rm e}^{{\rm i}\boldsymbol{k}\cdot\boldsymbol{r}_j}(\boldsymbol{\epsilon}\cdot\boldsymbol{p}_j)\right|\Psi_{\rm i}\right\rangle\right|^2 \times \delta(E_{\rm f} - E_{\rm i} - E), \quad (14)$$

where $|\Psi_{\rm i}\rangle$ and $|\Psi_{\rm f}\rangle$ are the wavefunctions at the final state and initial state, respectively. $E_{\rm i}$ and $E_{\rm f}$ are many-electron energies of the corresponding states. $\alpha = e^2/\hbar c \approx 1/137$ is the fine structure constant. In x-ray absorption spectroscopy, the wavelength of incident x-rays is much larger than the radius of the core wavefunction, i.e. $\boldsymbol{k}\cdot\boldsymbol{r} \ll 1$ and ${\rm e}^{{\rm i}\boldsymbol{k}\cdot\boldsymbol{r}} \approx 1$. Thus $\sigma_{\rm abs}$ can be evaluated to a good approximation as

$$\sigma_{\rm abs}(E) \approx \sum_{\rm f} 4\pi^2\alpha\,(E_{\rm f} - E_{\rm i}) \left|\left\langle \Psi_{\rm f}\left|\sum_{j=1}^{N} \boldsymbol{\epsilon}\cdot\boldsymbol{r}_j\right|\Psi_{\rm i}\right\rangle\right|^2 \times \delta(E_{\rm f} - E_{\rm i} - E) \quad (15)$$

which corresponds to an electric dipole transition. The commutation relations, $[\hat{H}, \boldsymbol{r}_j] = -i(\hbar/m)\boldsymbol{p}_j$, are used to obtain (15). In the case of 3d TM-$L_{2,3}$ XANES, the quadrupole transitions or the higher-order transitions are some hundred times weaker than the dipole transitions and can be neglected.

In atomic physics, the oscillator strength of the electric dipole transition is defined as

$$I_{\rm if} = \frac{2m}{\hbar^2}(E_{\rm f} - E_{\rm i}) \left|\left\langle \Psi_{\rm f}\left|\sum_{k=1}^{N} \boldsymbol{\epsilon}\cdot\boldsymbol{r}_k\right|\Psi_{\rm i}\right\rangle\right|^2. \quad (16)$$

Using (11), the bra–ket in (16) is evaluated by

$$\left\langle \Psi_{\rm f}\left|\sum_{k=1}^{N} \boldsymbol{\epsilon}\cdot\boldsymbol{r}_k\right|\Psi_{\rm i}\right\rangle = \sum_{p,q} C^*_{{\rm f}p} C_{iq} \sum_{k,l=1}^{M} (\boldsymbol{\epsilon}\cdot\langle k|\boldsymbol{r}|l\rangle)\langle\Phi_p|a_k^\dagger a_l|\Phi_q\rangle, \quad (17)$$

where $\langle k|\boldsymbol{r}|l\rangle$ denotes the dipole transition matrix element between one-electron states given by

$$\langle k|\boldsymbol{r}|l\rangle = \int \phi_k^*(\boldsymbol{r})\boldsymbol{r}\phi_l(\boldsymbol{r})\,{\rm d}\boldsymbol{r}. \quad (18)$$

Assigning (16) to (15) and replacing the Dirac δ function in (15) by the Lorentz function, $\sigma_{\rm abs}$ is expressed as

$$\sigma_{\rm abs}(E) = \sum_{\rm f} \frac{2\pi^2\hbar^2\alpha I_{\rm if}}{m}\frac{1}{2\pi}\frac{\Gamma}{[E - (E_{\rm f} - E_{\rm i})]^2 + \Gamma^2/4}. \quad (19)$$

The full width at half-maximum (FWHM) of the Lorentz function, Γ, in (19) corresponds to the broadening factor of peaks in the XANES spectrum. In general, each peak in an experimental TM-$L_{2,3}$ XANES spectrum has its own characteristic broadening [2]. Γ is determined by a variety of phenomena such as the core–hole lifetime, the Coster–Kronig Auger decay and the solid state (dispersion and vibration) effects, which are currently too complicated to estimate non-empirically. In general, the L_2-edge is broader than the L_3-edge due to the super-Coster–Kronig decay, where the L_2 hole decays to the L_3 hole. However, we use a constant value of Γ at all energy ranges to calculate the theoretical spectra for simplicity.

In the current procedure, the absolute transition energy, $E_{\rm f} - E_{\rm i}$, is overestimated by nearly 1%. This may come from the underestimation of electronic correlation due to the restriction of electronic configurations and the insufficient treatment of core–hole screening effects. In the present work, the absolute transition energy was corrected by taking the orbital energy difference between single-electron orbitals for Slater's transition state as a reference [11].

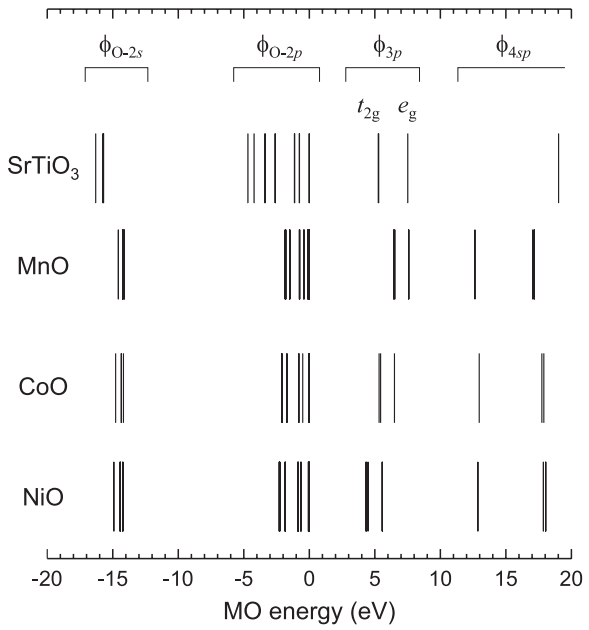

Figure 2. One-electron MO energy of TMO_6 clusters for $SrTiO_3$, MnO, CoO and NiO.

4. *Ab initio* multiplet calculations for TM-$L_{2,3}$ XANES

4.1. Molecular orbitals

As the first step of an *ab initio* CI calculation, a relativistic MO calculation is carried out using a model cluster composed of a TM ion and neighboring ligand ions within the local density approximation (LDA). The cluster is embedded into a mesh of point charges with formal valences, placed at the external atomic sites, so as to take into account the effective Madelung potential. Thus, the spatial distributions and the energy levels of MOs depend on the covalency between the TM ion and ligands, and the crystalline structure. Both crystal field effects and covalency between a TM ion and neighboring ligands can be included by using MOs. Therefore, this method can be applied to TM compounds with arbitrary atomic arrangement and symmetry.

Figure 2 shows the one-electron MO energies for $SrTiO_3$, MnO, CoO and NiO calculated by the RSCAT code [33]. In those calculations, TMO_6 clusters with octahedral (O_h) symmetry were used. In figure 2, the highest state of the $\phi_{O\ 2p}$ orbitals is set as the energy origin, where $\phi_{O\ 2p}$ denotes the molecular orbitals mainly composed of O 2p atomic orbitals. In those four compounds, the TM-3d levels split into two levels, namely t_{2g} and e_g, because of the ligand field. Strictly speaking, t_{2g} further splits because of the spin–orbit coupling at TM-3d levels. The expressions t_{2g} and e_g are not rigorously right within the relativistic theory. Instead, the representations of the double group, such as γ_{7g} and γ_{8g}, should be employed. However, the relativistic effects on TM-3d levels are small and the familiar expressions, t_{2g} and e_g, are used for simplicity. We define the ligand field splitting, 10 Dq, as the averaged energy difference between t_{2g} and e_g levels. 10 Dq as well as the spin–orbit splitting at core 2p levels, ξ_{2p}, are important factors

Table 1. Spin–orbit splitting on core 2p levels, ξ_{2p}, averaged energy difference between t_{2g} and e_g levels, i.e. 10 Dq, Mulliken's O 2p atomic orbital populations of t_{2g}, $Q_{O\ 2p}(t_{2g})$, and e_g, $Q_{O\ 2p}(e_g)$, and the difference between the Madelung potential for t_{2g} and e_g levels, ΔE^{MP} obtained by the relativistic MO calculations.

Compounds	ξ_{2p} (eV)	10 Dq (eV)	ΔE^{MP} (eV)	$Q_{O\ 2p}(t_{2g})$	$Q_{O\ 2p}(e_g)$
$SrTiO_3$	5.78	2.24	−0.26	0.083	0.126
MnO	10.44	1.10	0.20	0.022	0.083
CoO	14.84	1.14	0.27	0.027	0.111
NiO	17.50	1.19	0.35	0.033	0.143

to determine the multiplet structure and spectral shapes of TM-$L_{2,3}$ XANES. The values of ξ_{2p} and 10 Dq are summarized in table 1. In general, ξ_{2p} is the same when the atomic number of the TM ion is the same, and increases with the increase in atomic number. In contrast, 10 Dq depends on the chemical state of TM ions, covalency between TM ions and ligands, and the Madelung potential. The contribution of the Madelung potential on 10 Dq, i.e. ΔE^{MP}, can be calculated as

$$\Delta E^{MP} = \langle e_g|v_{ext}|e_g\rangle - \langle t_{2g}|v_{ext}|t_{2g}\rangle. \qquad (20)$$

The evaluated values of ΔE^{MP} are also listed in table 1. One can see that ΔE^{MP} contributes a few tens of percentage points of 10 Dq. The result indicates that ignoring the Madelung potential can cause large errors in the ligand field splitting, and thus the multiplet structure in TM-$L_{2,3}$ XANES [34]. The dependences of the Madelung potential on the crystal structure and their contribution to the Co $L_{2,3}$ XANES were discussed in detail by Kumagai *et al* [35]. The relative energies of the ϕ_{3d} levels with respect to the $\phi_{O\ 2p}$ levels are also important for the TM-$L_{2,3}$ XANES, since charge transfer can occur when the energy difference between these two levels is small. In general, the energy difference between ϕ_{3d} levels and $\phi_{O\ 2p}$ decreases as the atomic number of TM increases. It also decreases when the number of 3d electrons decreases because the system with the smaller 3d electrons has less inter-electron repulsion. These tendencies can be seen in figure 2.

4.2. Covalency and reduction of two-electron integrals

The multiplet levels are obtained by diagonalizing the many-electron Hamiltonian matrix (12). Thus, the multiplet energies depend on the one-electron integrals (8), which describe the ligand field splitting and the hopping integrals among MOs, and the two-electron integrals (9), which denote the inter-electron interaction energies. In the *ab initio* CI calculation, those integrals are directly evaluated over the MOs. Thus, we can obtain the multiplet levels without any empirical parameters. In order to make the initial and final states orthogonal, both initial and final states were described using the same MO set in the present calculations. In other words, the values of one- and two-electron integrals were the same in both initial and final states. The change of covalency in the final states due to the existence of a core–hole was not considered. The core–hole effects were taken into account only through the CI. The effects of MO relaxation at the final states on the multiplet states were discussed by Bagus and Ilton [36].

The Coulomb repulsion between the TM-2p hole and the TM-3d electrons (holes) of an isolated TM ion is reduced when the TM ion forms bonds with the ligand ions in solids. In the case of 3d TM oxides, there exist strong covalent bonding between the TM-3d and the O 2p orbitals. In table 1, the contribution of O 2p atomic orbitals to the t_{2g} and the e_g levels evaluated by Mulliken's population analysis method [37] is also shown. In all oxides, the O 2p population ($Q_{O\ 2p}$) is much greater in e_g than in t_{2g}. The magnitude of Coulomb repulsion among electrons is determined by the two-electron integrals $\langle ij|\hat{g}|kl\rangle$, where $\hat{g}$ is the Coulomb interaction operator. The calculated two-electron integrals for four oxides, i.e. $SrTiO_3$, MnO, CoO and NiO, and for the isolated ions with the same formal charges are listed in table 2. Although we obtained the values of all two-electron integrals, only the averaged value of Coulomb integrals:

$$U_{\mathrm{ave}}(P, Q) = \frac{1}{2K} \sum_{i,j \in P,Q} \langle ij\,|\hat{g}|\,ij\rangle, \tag{21}$$

are shown for simplicity, where P and Q denote the set of orbitals, i.e. $2p_{1/2}$, $2p_{3/2}$ or 3d for the isolated ions, and $\phi_{2p1/2}$, $\phi_{2p3/2}$, t_{2g} or e_g for TM oxides. K is the number of integrals summed. The values inside the parentheses of table 2 are the ratios between the averaged Coulomb integrals of TMO_6 clusters to those of isolated TM ions. The atomic value of U_{ave} can be decomposed as the sum of several Slater integrals, F^k: F^0 and F^2 are included for $U_{\mathrm{ave}}(2p, 2p)$ and $U_{\mathrm{ave}}(2p, 3d)$, and F^0, F^2 and F^4 for $U_{\mathrm{ave}}(3d, 3d)$. In the case of the solid state, however, many more Slater integrals are required to describe U_{ave} because of the breaking of spherical symmetry. Therefore, the Slater integrals are not explicitly calculated in the *ab initio* CI method. Instead, the two-electron integrals over MOs, $\langle ij|\hat{g}|kl\rangle$, are directly evaluated by numerical integration.

From table 2, one can clearly see that $U_{\mathrm{ave}}(\phi_{2p}, \phi_{2p})$ in TM oxides are almost the same as $U_{\mathrm{ave}}(2p, 2p)$ in isolated ions. This is because the core 2p levels are hardly affected by the ligand field. In contrast, $U_{\mathrm{ave}}(\phi_{2p}, \phi_{3d})$ and $U_{\mathrm{ave}}(\phi_{3d}, \phi_{3d})$ in TM oxides are significantly reduced from the atomic values, $U_{\mathrm{ave}}(2p, 3d)$ and $U_{\mathrm{ave}}(3d, 3d)$. The reduction of 3d–3d Coulomb interactions is larger than that of 2p–3d interactions. The reduction of Coulomb integrals becomes larger when the covalent bonding between TM-3d and O 2p orbitals is large. For instance, $U_{\mathrm{ave}}(e_g, e_g)$ is more reduced than $U_{\mathrm{ave}}(t_{2g}, t_{2g})$ from the corresponding values of isolated ions. This is because, when the mixing of TM-3d and O 2p orbitals is larger, the effective spatial region where electrons can move is spread wider, hence the Coulomb repulsion becomes smaller.

It should be noted that, in charge transfer multiplet theory, the Slater integrals, which determine the inter-electron interaction, are taken at their atomic values in most calculations of TM compounds. If the Hartree–Fock method is used to calculate them, the atomic values identify with a 20% reduction of the Hartree–Fock values. The reductions in the two-electron integrals due to covalency are neglected in CTM theory, or they are, uniformly, empirically imposed.

Table 2. Averaged values of the Coulomb integrals $\langle ij|1/r_{12}|ij\rangle (i \neq j)$ in eV among TM-$2p_{1/2}$, $2p_{3/2}$ and 3d (t_{2g}, e_g) orbitals for TMO_6 clusters and isolated TM ions. The values inside parentheses indicate the reduction factors of the Coulomb integrals from the corresponding atomic values.

U_{ave}	Ti^{4+}	$SrTiO_3$	Mn^{2+}	MnO
($2p_{1/2}$, $2p_{1/2}$)	86.34	86.29 (0.999)	101.39	101.33 (0.999)
($2p_{1/2}$, $2p_{3/2}$)	85.93	85.88 (0.999)	100.77	100.70 (0.999)
($2p_{3/2}$, $2p_{3/2}$)	84.99	84.95 (1.000)	99.54	99.47 (0.999)
($2p_{1/2}$, 3d)	29.62		31.64	
($2p_{1/2}$, t_{2g})		26.38 (0.891)		30.45 (0.962)
($2p_{1/2}$, e_g)		26.21 (0.885)		29.74 (0.940)
($2p_{3/2}$, 3d)	29.61		31.63	
($2p_{3/2}$, t_{2g})		26.37 (0.891)		30.44 (0.962)
($2p_{3/2}$, e_g)		26.20 (0.885)		29.73 (0.940)
(3d, 3d)	21.86		22.46	
(t_{2g}, t_{2g})		18.47 (0.845)		21.30 (0.948)
(t_{2g}, e_g)		17.96 (0.822)		20.44 (0.908)
(e_g, e_g)		17.83 (0.816)		20.03 (0.892)
U_{ave}	Co^{2+}	CoO	Ni^{2+}	NiO
($2p_{1/2}$, $2p_{1/2}$)	111.47	111.40 (0.999)	116.54	116.45 (0.999)
($2p_{1/2}$, $2p_{3/2}$)	110.67	110.60 (0.999)	115.64	115.55 (0.999)
($2p_{3/2}$, $2p_{3/2}$)	109.21	109.14 (0.999)	114.05	113.97 (0.999)
($2p_{1/2}$, 3d)	35.50		37.43	
($2p_{1/2}$, t_{2g})		34.24 (0.965)		36.09 (0.964)
($2p_{1/2}$, e_g)		32.75 (0.923)		33.72 (0.901)
($2p_{3/2}$, 3d)	35.48		37.41	
($2p_{3/2}$, t_{2g})		34.23 (0.964)		36.07 (0.964)
($2p_{3/2}$, e_g)		32.74 (0.900)		33.70 (0.900)
(3d, 3d)	25.10		26.42	
(t_{2g}, t_{2g})		23.80 (0.948)		24.98 (0.945)
(t_{2g}, e_g)		22.44 (0.894)		23.06 (0.872)
(e_g, e_g)		21.58 (0.860)		21.75 (0.823)

4.3. Multiplet structures and transition probabilities

The multiplet structures corresponding to TM-$L_{2,3}$ XANES for $SrTiO_3$, MnO and CoO have been calculated by the *ab initio* CI method or, strictly speaking, the DFT–CI method. In these calculations, TMO_6 clusters embedded in the Madelung potential were used. The one-electron and the two-electron integrals among ϕ_{2p}, ϕ_{3d} and $\phi_{O\ 2p}$ were explicitly calculated, while the interactions with the electrons occupying other orbitals were treated as the effective potential with LDA. As mentioned in section 3.3, the CI calculations were carried out with restricted configurations. TM-$L_{2,3}$ XANES can be mainly ascribed to the transition from the $(\phi_{2p})^6(\phi_{3d})^n$ configuration to the $(\phi_{2p})^5(\phi_{3d})^{n+1}$ configuration. Thus, only ϕ_{2p} ($2p_{1/2}$, $2p_{3/2}$) and ϕ_{3d} (t_{2g}, e_g) MOs were taken as the active space. In other words, only the configurations obtained by changing the occupation in those 16 MOs were used to expand many-electron wavefunctions. $\phi_{O\ 2p}$ orbitals (36 MOs) were fully occupied in those Slater determinants. Moreover, the configurations having two or more holes on ϕ_{2p} orbitals were not considered, because the many-electron energies of such configurations are much higher and they do not significantly interact with these two configurations described above.

In the case of Ti $L_{2,3}$ XANES of $SrTiO_3$, for instance, the initial configuration is $(\phi_{2p_{1/2}})^2(\phi_{2p_{3/2}})^4(t_{2g})^0(e_g)^0$, which can provide only a single Slater determinant. On the other hand, the final configuration $(\phi_{2p_{1/2}})^2(\phi_{2p_{3/2}})^4(t_{2g})^1(e_g)^0$ can

Table 3. Occupation numbers of each level of orbitals for the initial and final configurations for the TM-$L_{2,3}$ XANES for $SrTiO_3$, MnO and CoO, and the number of Slater determinants.

		$\phi_{2p_{1/2}}$	$\phi_{2p_{3/2}}$	t_{2g}	e_g	N_{SD}	Total
$SrTiO_3$	Initial	2	4	0	0	1	1
	Final	2	3	1	0	24	60
		2	3	0	1	16	
		1	4	1	0	12	
		1	4	0	1	8	
MnO	Initial	2	4	5	0	6	252
		2	4	4	1	60	
		2	4	3	2	120	
		2	4	2	3	60	
		2	4	1	4	6	
	Final	2	3	6	0	4	1260
		2	3	5	1	96	
		2	3	4	2	360	
		2	3	3	3	320	
		2	3	2	4	60	
		1	4	6	0	2	
		1	4	5	1	48	
		1	4	4	2	180	
		1	4	3	3	160	
		1	4	2	4	30	
CoO	Initial	2	4	6	1	4	120
		2	4	5	2	36	
		2	4	4	3	60	
		2	4	3	4	20	
	Final	2	3	6	2	24	270
		2	3	5	3	96	
		2	3	4	4	60	
		1	4	6	2	12	
		1	4	5	3	48	
		1	4	4	4	30	

make $24(={}_4C_3 \times {}_6C_1)$ Slater determinants. Including the other three configurations, 60 Slater determinants can be made for the final states. The electronic configurations corresponding to the initial and final states of TM-$L_{2,3}$ XANES for these three oxides and the number of Slater determinants are summarized in table 3.

The many-electron energies and the many-electron wavefunctions were calculated by diagonalizing the many-electron Hamiltonian (13). The bottom panels in figure 3 show the multiplet structures corresponding to the final states of TM-$L_{2,3}$ XANES of $SrTiO_3$, MnO and CoO. The number of final states for these three oxides are 60, 1260 and 270, respectively. Though a Ti ion in $SrTiO_3$ is in a d^0 configuration at the ground state, the final states of Ti $L_{2,3}$ XANES shows widespread multiplet structure because of the strong Coulomb interactions between ϕ_{2p} core–hole and the excited electron. More complicated multiplet structures can be seen in the case of MnO and CoO, because of the interactions among the ϕ_{2p} core–hole, the excited electron and the pre-existing ϕ_{3d} electrons. The oscillator strengths of the electric dipole transitions and the PACS were evaluated using equations (16) and (19), respectively. The FWHM of the Lorentz functions were set to 0.6 eV over the whole energy region. The results are shown in the middle panels in figure 3. They are compared with the experimental spectra taken from the literature [38–40] (upper panels). One can clearly see that only a part of the multiplet states contribute to the TM-$L_{2,3}$ spectra. This is because of the selection rule of the electronic dipole transition. The theoretical spectra of these three compounds show good agreement with the experimental spectra. The peak positions and the intensity ratios, and the small shoulder peaks, are well reproduced.

4.4. Charge transfer effects in the ab initio CI method

The charge transfer (CT) from ligand ions to the TM ions plays an important role in the spectral shapes of the TM-$L_{2,3}$ XANES of some 3d TM compounds. In the CTM approach, the charge transfer effects are treated as the configuration interaction among two (or more) atomic configurations as described in section 2.3.

The 'charge transfer' effects in the CTM approach are divided into two parts in the *ab initio* CI method based on MOs. The first part is the charge transfer through the covalent bonding between the TM-3d and ligand orbitals, which can automatically be included using MOs instead of atomic orbitals (AOs). The other part is the additional electronic excitation from the MOs corresponding to the valence band to ϕ_{3d} orbitals. This contribution can be included by taking the additional configurations (Slater determinants) in the CI. In this section, we use the phrase, 'charge transfer', to indicate the latter effect.

The charge transfer multiplet structures of TM-$L_{2,3}$ XANES for $SrTiO_3$ and NiO have been calculated using TMO_6 clusters with the DFT–CI method. Similar to LF multiplet calculations, the one-electron and the two-electron integrals among ϕ_{2p}, ϕ_{3d} and $\phi_{O\ 2p}$ were explicitly calculated, while the interactions with the electrons occupying other orbitals were treated as the effective potential with LDA. The charge transferred configurations $(\phi_{3d})^{n+1}(\phi_{O\ 2p})^{-1}$ and $(\phi_{2p})^5(\phi_{3d})^{n+2}(\phi_{O\ 2p})^{-1}$ were added to describe the initial and the final states, respectively, where $(\phi_{O\ 2p})^{-1}$ denotes a hole in $\phi_{O\ 2p}$ orbitals. In those calculations, the $36(=6 \times 6)$ neighboring $\phi_{O\ 2p}$ orbitals were explicitly considered as ligand orbitals. Thus, the charge-transferred configurations described above were explicitly described as $(\phi_{2p})^6(\phi_{3d})^{n+1}(\phi_{O\ 2p})^{35}$ and $(\phi_{2p})^5(\phi_{3d})^{n+2}(\phi_{O\ 2p})^{35}$. The electronic configurations considered in the calculations and the numbers of Slater determinants were summarized in table 4. As can be seen, the number of Slater determinants, and hence the dimension of the Hamiltonian matrix, drastically increase by including the CT. In the CTM model, the charge transfer energy, Δ, and the hopping integrals between ligand state and 3d, T, are introduced as additional empirical parameters to describe the energy levels. Δ determines the relative energy of $3d^{n+1}\underline{L}$ to $3d^n$ multiplet levels, while T controls the mixing between $3d^{n+1}\underline{L}$ and $3d^n$ configurations. The charge transfer energy at the final state is changed by $U_{3d3d} - U_{2p3d}$, where U_{3d3d} and U_{2p3d} denote the on-site Coulomb interaction between two 3d electrons and that between a 2p core–hole and a 3d electron, respectively. In the *ab initio* CI method, the contributions of those parameters are automatically and rigorously included in the Hamiltonian matrix. The energy difference between

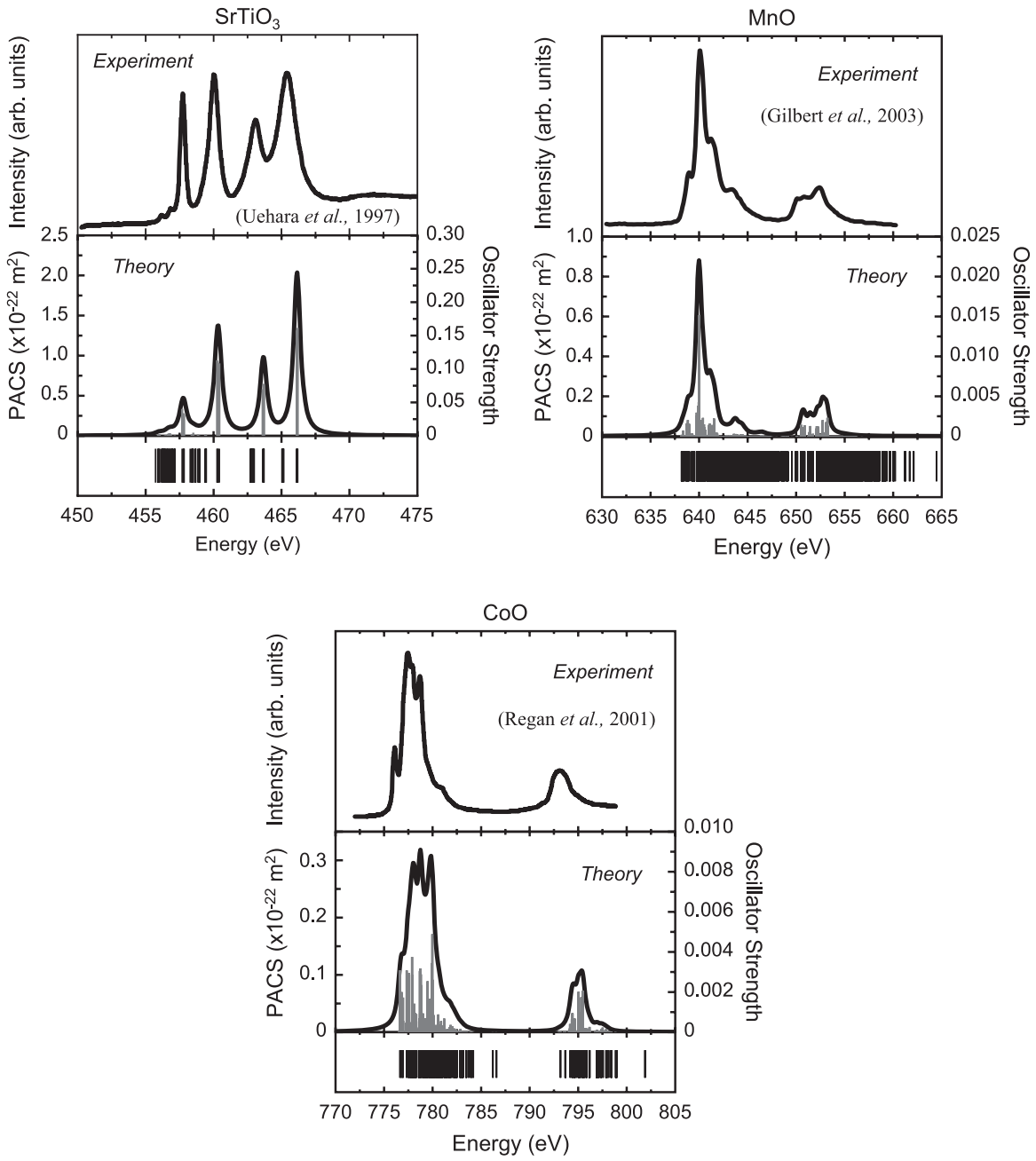

Figure 3. Multiplet levels (bottom) and theoretical spectra of TM-$L_{2,3}$ XANES (middle) for $SrTiO_3$, MnO and CoO compared with experimental ones taken from the literature [38–40] (top). The gray bars drawn with theoretical spectra are the oscillator strengths of electric dipole transitions.

$(\phi_{3d})^n$ and $(\phi_{3d})^{n+1}(\phi_{O\ 2p})^{-1}$ configurations can be described as the difference of the Hamiltonian matrix elements $\langle\Phi_{LF}|\hat{H}|\Phi'_{LF}\rangle$ and $\langle\Phi_{CT}|\hat{H}|\Phi'_{CT}\rangle$, where Φ_{LF} and Φ_{CT} represent the Slater determinants belonging to the original and the charge-transferred configurations, respectively. $(\phi_{3d})^n$ and $(\phi_{3d})^{n+1}(\phi_{O\ 2p})^{-1}$ configurations are mixed when the non-diagonal block $[\langle\Phi_{LF}|\hat{H}|\Phi_{CT}\rangle]$ has non-zero elements. Since all one- and two-electron integrals are already evaluated, the matrix elements, $\langle\Phi_{LF}|\hat{H}|\Phi'_{LF}\rangle$, $\langle\Phi_{CT}|\hat{H}|\Phi'_{CT}\rangle$ and $\langle\Phi_{LF}|\hat{H}|\Phi_{CT}\rangle$, can be evaluated using (12) without any empirical parameters. The values of those matrix elements are different because of the difference of the coupling coefficients, $\langle\Phi_p|a_i^\dagger a_j|\Phi_q\rangle$ and $\langle\Phi_p|a_i^\dagger a_j^\dagger a_l a_k|\Phi_q\rangle$, which depend on the difference of the orbital occupation corresponding to the Slater determinants Φ_p and Φ_q. The contribution of $U_{3d3d} - U_{2p3d}$ in the charge transfer energy at the final states is also explicitly included in the Hamiltonian matrix for the final configurations. Thus, the CT multiplet levels can be obtained by just diagonalizing the enlarged Hamiltonian matrix.

It should be noted that the number of ligand orbitals depends on the ligand atoms and the coordination number in the *ab initio* CI method. For instance, we only use $24(=6 \times 4)\phi_{O\ 2p}$ orbitals in the case of a TMO_4 cluster. In addition,

Table 4. Occupation numbers of each level of orbitals for the initial and final configurations for the TM-$L_{2,3}$ XANES of NiO and $SrTiO_3$ including the charge transfer.

		$\phi_{2p_{1/2}}$	$\phi_{2p_{3/2}}$	t_{2g}		e_g	N_{SD}	Total
$SrTiO_3$	Initial	2	4	36	0	0	1	
	Initial	2	4	35	1	0	216	361
	(CT)	2	4	35	0	1	144	
	Final	2	3	36	1	0	24	
		2	3	36	0	1	16	
		1	4	36	1	0	12	
		1	4	36	0	1	8	
NiO	Final	2	3	35	2	0	2160	9780
	(CT)	2	3	35	1	1	3456	
		2	3	35	0	2	864	
		1	4	35	2	0	1080	
		1	4	35	1	1	1728	
		1	4	35	0	2	432	
	Initial	2	4	36	6	2	6	405
		2	4	36	5	3	24	
		2	4	36	4	4	15	
	Initial	2	4	35	6	3	144	
	(CT)	2	4	35	5	4	216	
	Final	2	3	36	6	3	16	276
		2	3	36	5	4	24	
		1	4	36	6	3	8	
		1	4	36	5	4	12	
	Final	2	3	35	6	4	144	
	(CT)	1	4	35	6	4	72	

each ligand orbital has different excitation energy and coupling strength. In other words, multiple charge transfer channels are taken into account in the *ab initio* CI method. They are the big differences between the *ab initio* CI method and the CTM model. In the CTM model, a ligand hole is described as a delocalized 3d wavefunction (see section 2.3), and the same excitation energy and coupling strength are used in most cases.

It should also be noted that, in principle, two or more ligand metal CT channels or metal ligand CT can be included by taking the corresponding electronic configurations in the *ab initio* CI method. The metal–metal CT can be included if we use a cluster model including multiple TM ions and take the additional electronic configuration corresponding to the metal–metal CT in the CI. In practice, this approach is only available for a small number of systems since, in most cases, the number of Slater determinants, i.e. the size of the Hamiltonian matrix, becomes too large to solve with the present computational power.

Figures 4 and 5 show the theoretical TM-$L_{2,3}$ XANES of $SrTiO_3$ and NiO, respectively, calculated by the DFT–CI method without the CT configurations (b) and with CT configurations (c). The former calculation includes only the ligand field (LF) effects, while the latter one does include both LF effects and CT effects. Here, we refer to these two types of calculations as the 'LF multiplet' approach and 'LF + CT multiplet' approach, respectively. They are compared with experimental spectra (a). One can clearly observe that, in both oxides, the spectral shapes change by including the CT from $\phi_{O\,2p}$ to ϕ_{3d} orbitals. In the case of $SrTiO_3$, the L_2 peaks are much more broadened by the CT, though the constant

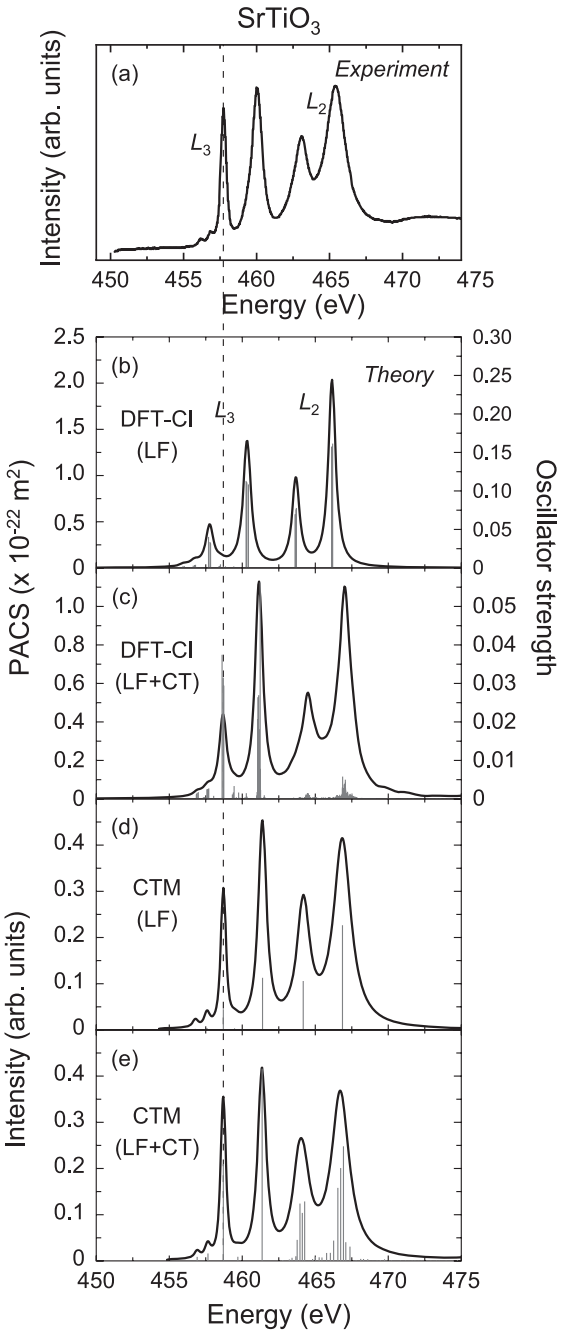

Figure 4. Experimental spectrum of Ti $L_{2,3}$ XANES for $SrTiO_3$ taken from [38] (a) compared with four different theoretical spectra: (b) ligand field multiplet calculation by the DFT–CI method, (c) charge transfer multiplet calculation by the DFT–CI method, (d) ligand field multiplet calculation by the CTM method ($10Dq = 2.5$ eV) and (e) charge transfer multiplet calculation by the CTM method ($10Dq = 2.2$ eV, $\Delta = 4$ eV, $U_{2p3d} - U_{3d3d} = 2$ eV, hopping $V(e_g) = 2$ eV). Solid bars drawn with theoretical spectra are the oscillator strengths for the many-electron eigenstates. The theoretical spectra in (d) and (e) are shifted so as to align the first main peak of the L_3-edge with that in (c).

broadening factor is used in the calculation. In the case of NiO, the L_3/L_2 intensity ratio, i.e. the branching ratio, significantly decreases by including the CT. The double peak feature on the L_2-edge becomes much clearer, and the small satellite

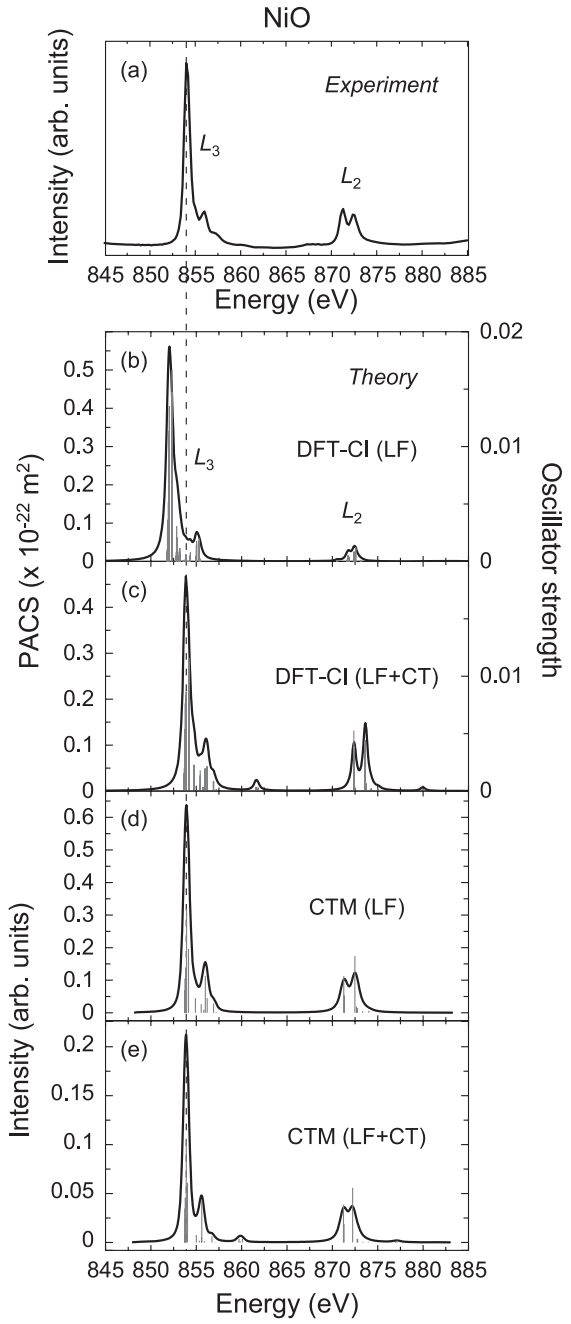

Figure 5. Experimental spectrum of Ni $L_{2,3}$ XANES for NiO (a) compared with four different theoretical spectra: (b) ligand field multiplet calculation by the DFT–CI method, (c) charge transfer multiplet calculation by the DFT–CI method, (d) ligand field multiplet calculation by the CTM method ($10Dq = 1.2$ eV) and (e) charge transfer multiplet calculation by the CTM method ($10Dq = 0.9$ eV, $\Delta = 3.5$ eV, $U_{2p3d} - U_{3d3d} = 1$ eV, hopping $V(e_g) = 2$ eV). Solid bars drawn with theoretical spectra are the oscillator strengths for the many-electron eigenstates. The theoretical spectra in (d) and (e) are shifted so as to align the first main peak of the L_3-edge with that in (c).

peaks appear at the higher energy region of both L_3- and L_2-edges in the LF + CT multiplet approach. In both oxides, the theoretical spectra from the LF + CT multiplet approach show better agreement with the experimental results than those from the LF multiplet approach.

Table 5. Composition of each electronic configuration at the initial states of TM-$L_{2,3}$ XANES.

	Configuration	Composition
$SrTiO_3$ (LF)	$(\phi_{O\ 2p})^{36}(t_{2g})^0(e_g)^0$	1.000
$SrTiO_3$	$(\phi_{O\ 2p})^{36}(t_{2g})^0(e_g)^0$	0.950
(LF + CT)	$(\phi_{O\ 2p})^{35}(t_{2g})^1(e_g)^0$	0.036
	$(\phi_{O\ 2p})^{35}(t_{2g})^0(e_g)^1$	0.014
NiO	$(\phi_{O\ 2p})^{36}(t_{2g})^6(e_g)^2$	0.591
(LF)	$(\phi_{O\ 2p})^{36}(t_{2g})^5(e_g)^3$	0.390
	$(\phi_{O\ 2p})^{36}(t_{2g})^4(e_g)^4$	0.018
NiO	$(\phi_{O\ 2p})^{36}(t_{2g})^6(e_g)^2$	0.913
(LF + CT)	$(\phi_{O\ 2p})^{36}(t_{2g})^5(e_g)^3$	0.003
	$(\phi_{O\ 2p})^{36}(t_{2g})^4(e_g)^4$	0.000
	$(\phi_{O\ 2p})^{35}(t_{2g})^6(e_g)^3$	0.084
	$(\phi_{O\ 2p})^{36}(t_{2g})^5(e_g)^4$	0.000

In order to investigate the CT effects in detail, configuration analysis of many-electron wavefunctions has been carried out. Considering the orthonormality of the Slater determinants, the composition of the pth Slater determinant in the kth eigenstate is simply given by $|C_{pk}|^2$. Table 5 shows the compositions of each electronic configuration at the initial state of TM-$L_{2,3}$ XANES for $SrTiO_3$ and NiO. In the case of $SrTiO_3$, the initial state obtained by the LF multiplet approach is completely composed of the $(t_{2g})^0(e_g)^0$ configuration. In the LF + CT multiplet approach, the initial state is still dominated by the $(t_{2g})^0(e_g)^0$ configuration, whose composition at the initial state is 95.0%. The contributions of the charge transfer configurations, $(t_{2g})^1(e_g)^0(\phi_{O\ 2p})^{-1}$ and $(t_{2g})^0(e_g)^1(\phi_{O\ 2p})^{-1}$, are small.

In the case of NiO, in contrast, the contribution of each configuration is significantly changed when the CT is included. In the one-electron scheme, the initial configuration of NiO can be described as 100% $(t_{2g})^6(e_g)^2$. The result of the LF + CT multiplet approach shows that the contribution of the $(t_{2g})^6(e_g)^2$ configuration increases to 91.3% at the initial state. The charge transfer configuration, $(t_{2g})^6(e_g)^3(\phi_{O\ 2p})^{-1}$, also contributes 8.4% at the initial state. Although we will take account of all configurations for the XANES calculations to describe the initial state, the $(t_{2g})^6(e_g)^2$ configuration is found to be predominant, which agrees well with our intuition.

On the other hand, the result of the LF multiplet approach shows that the contribution of $(t_{2g})^6(e_g)^2$ is only 59.1%. The $(t_{2g})^6(e_g)^2$ configuration strongly interacts with the $(t_{2g})^5(e_g)^3$ configuration, whose composition is 39.0% at the initial state. The large discrepancies in the two theoretical spectra can be ascribed to the difference of the $(t_{2g})^5(e_g)^3$ composition at the initial states. This result is far from our intuition, and is physically unreliable. This is because of the strong restriction of electronic configurations. In the LF multiplet approach, the electronic correlations among the ligand hole and ϕ_{3d} electrons, which contribute to reduce the total inter-electron interaction energies, are completely neglected. The abnormally large contribution of $(t_{2g})^5(e_g)^3$ in the LF multiplet result may have occurred to reduce the inter-electron interaction in the spatially localized ϕ_{3d} orbitals within the restricted electronic configurations. In fact, the Coulomb interaction among t_{2g} is much larger than that among e_g or that between t_{2g} and

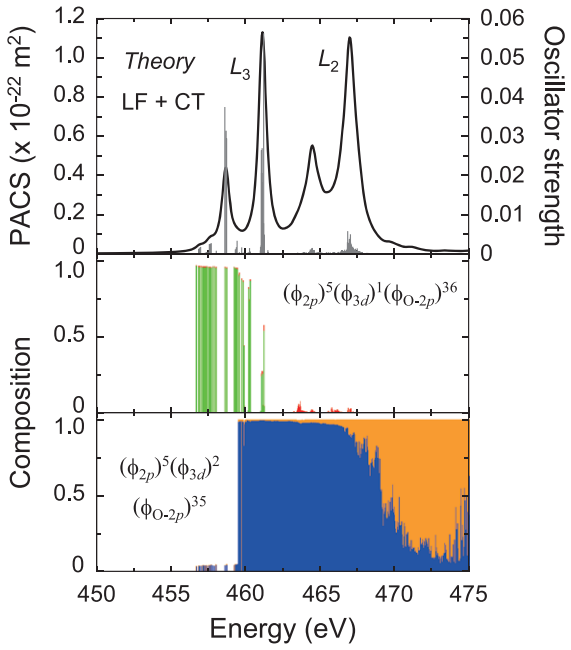

Figure 6. Theoretical Ti $L_{2,3}$ XANES of $SrTiO_3$ by the DFT–CI method including the charge transfer. Middle and lower panels show the compositions of $(\phi_{2p})^5(\phi_{O\ 2p})^{36}(\phi_{3d})^1$ and $(\phi_{2p})^5(\phi_{O\ 2p})^{35}(\phi_{3d})^2$ configurations for the many-electron eigenstates, respectively, where the contributions of L_3 and L_2 configurations are distinguished by the different colors. (In the online version, the compositions of four final configurations are distinguished by the different colors: green $(\phi_{2p_{1/2}})^2(\phi_{2p_{3/2}})^3(\phi_{O\ 2p})^{36}(\phi_{3d})^1$, red $(\phi_{2p_{1/2}})^1(\phi_{2p_{3/2}})^4(\phi_{O\ 2p})^{36}(\phi_{3d})^1$, blue $(\phi_{2p_{1/2}})^2(\phi_{2p_{3/2}})^3(\phi_{O\ 2p})^{35}(\phi_{3d})^2$ and orange $(\phi_{2p_{1/2}})^1(\phi_{2p_{3/2}})^4(\phi_{O\ 2p})^{35}(\phi_{3d})^2$.)

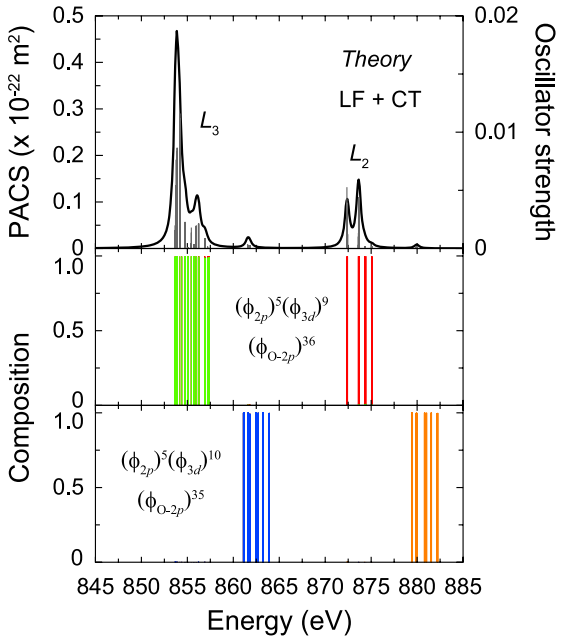

Figure 7. Theoretical Ni $L_{2,3}$ XANES of NiO by the DFT–CI method including the charge transfer. Middle and lower panels show the compositions of $(\phi_{2p})^5(\phi_{O\ 2p})^{36}(\phi_{3d})^9$ and $(\phi_{2p})^5(\phi_{O\ 2p})^{35}(\phi_{3d})^{10}$ configurations for the many-electron eigenstates, respectively, where the contributions of L_3 and L_2 configurations are distinguished by the different colors. (In the online version, the compositions of four final configurations are distinguished by the different colors: green $(\phi_{2p_{1/2}})^2(\phi_{2p_{3/2}})^3(\phi_{O\ 2p})^{36}(\phi_{3d})^9$, red $(\phi_{2p_{1/2}})^1(\phi_{2p_{3/2}})^4(\phi_{O\ 2p})^{36}(\phi_{3d})^9$, blue $(\phi_{2p_{1/2}})^2(\phi_{2p_{3/2}})^3(\phi_{O\ 2p})^{35}(\phi_{3d})^{10}$ and orange $(\phi_{2p_{1/2}})^1(\phi_{2p_{3/2}})^4(\phi_{O\ 2p})^{35}(\phi_{3d})^{10}$.)

e_g (see table 2). The CT configurations are indispensable to describe the initial state properly in the case of NiO.

It should be noted that the composition of the charge transfer configuration, $(\phi_{2p})^6(\phi_{O\ 2p})^{35}(\phi_{3d})^{n+1}$, at the initial state in the LF + CT multiplet approach is much smaller than the composition of $(2p)^6(3d)^{n+1}\underline{L}$ in the charge transfer multiplet theory. This is because the covalency is already included by using the MOs (ϕ_{3d}) instead of AOs (3d) in the former case, while that is included through the mixing of the $(2p)^6(3d)^{n+1}\underline{L}$ configuration in the latter case.

The charge transfer configurations also contribute to the final state of TM-$L_{2,3}$ XANES. Figures 6 and 7 show the contribution of the $(\phi_{2p})^5(\phi_{O\ 2p})^{36}(\phi_{3d})^{n+1}$ and $(\phi_{2p})^5(\phi_{O\ 2p})^{35}(\phi_{3d})^{n+2}$ configurations at the final states for $SrTiO_3$ and NiO in the LF + CT multiplet approach. The contributions of L_3 and L_2 configurations are distinguished by the different colors. The calculated PACS and the oscillator strengths are also shown in the top panels. Although only a part of these components significantly contribute to the oscillator strength, the diagram is quite useful for a detailed analysis of the spectral shape.

In the case of $SrTiO_3$, the number of final states for Ti $L_{2,3}$ is 9780. Almost semi-continuous multiplet levels can be seen in figure 6. The eigenstates below 460 eV, which are responsible for the first main peak at the L_3-edge and the small shoulder peaks located at the lower energy region, are predominantly composed by the $(\phi_{2p3/2})^{-1}(\phi_{3d})^1$ (lighter-colored bars in the middle panel) configuration. The small contribution of the $(\phi_{2p3/2})^{-1}(\phi_{3d})^2(\phi_{O\ 2p})^{-1}$ (darker-colored bars in the lower panel) configuration is found in this region. In contrast, the eigenstates above 460 eV are predominantly composed by the $(\phi_{2p3/2})^{-1}(\phi_{3d})^2(\phi_{O\ 2p})^{-1}$ (darker-colored bars in the lower panel) and $(\phi_{2p1/2})^{-1}(\phi_{3d})^2(\phi_{O\ 2p})^{-1}$ (lighter-colored bars in the lower panel) configurations. In particular, at the eigenstates which are responsible for the L_2 peaks (462–470 eV), the composition of the $(\phi_{2p1/2})^{-1}(\phi_{3d})^1$ configuration (darker-colored bars in the middle panel), which is a dipole-allowed configuration from the $(\phi_{3d})^0$ configuration, becomes significantly smaller in this energy region. In fact, the composition of the $(\phi_{2p1/2})^{-1}(\phi_{3d})^1$ configuration is at most 8%, and smaller than 4% in most states. Hence, the oscillator strength at each eigenstate in this energy region becomes much smaller than those in the case of the LF multiplet approach (see figure 3). In the case of the LF + CT multiplet approach, however, many more numbers of eigenstates contribute to the Ti L_2 peaks, and they are widely distributed in the range 463–468 eV. As a result of this, the L_2 peaks are much broadened compared with those calculated by the LF multiplet approach.

The contribution of the CT at the final states is much simpler in the case of NiO than $SrTiO_3$. The number of final states for Ni $L_{2,3}$ XANES is only 276 even including the CT configurations. One can hardly see the interaction among the four configurations, i.e. $(\phi_{2p3/2})^{-1}(\phi_{3d})^9$, $(\phi_{2p3/2})^{-1}(\phi_{3d})^{10}(\phi_{O\ 2p})^{-1}$, $(\phi_{2p1/2})^{-1}(\phi_{3d})^9$ and $(\phi_{2p1/2})^{-1}$

$(\phi_{3d})^{10}(\phi_{O\ 2p})^{-1}$ in figure 7. The main structures of the L_3- and L_2-edges are purely composed by $(\phi_{2p3/2})^{-1}(\phi_{3d})^9$, and $(\phi_{2p1/2})^{-1}(\phi_{3d})^9$, configurations, respectively. The charge transfer configurations only contribute to form the small satellite peaks. It is noteworthy that the eigenstates which are responsible for the satellite peak located around 862 eV (880 eV) are 100% composed of $(\phi_{2p3/2})^{-1}(\phi_{3d})^{10}(\phi_{O\ 2p})^{-1}$ ($(\phi_{2p1/2})^{-1}(\phi_{3d})^{10}(\phi_{O\ 2p})^{-1}$) configurations. The electric dipole transition from $(\phi_{3d})^8$ to this configuration is not allowed. The dipole transition from the $(\phi_{3d})^9(\phi_{O\ 2p})^{-1}$ configuration, which is the minor component at the initial state of NiO, contributes to the oscillator strengths. Therefore, the CT effects both at initial and final states contribute to the formation of the satellite peaks in Ni $L_{2,3}$ XANES.

Note again that in the CTM model the large mixing between $(2p)^5(3d)^9$ and $(2p)^5(3d)^{10}\underline{L}$ is found at the final states of Ni $L_{2,3}$ XANES [41]. In the *ab initio* CI method based on MOs, the mixing between $(2p)^5(3d)^9$ and $(2p)^5(3d)^{10}\underline{L}$ has been included as the covalent bonding between Ni 3d and O 2p orbitals.

4.5. Comparison between the ab initio CI method and the CTM method

In figures 4 and 5, theoretical TM-$L_{2,3}$ XANES of $SrTiO_3$ and NiO obtained by the LF multiplet (d) and the CT multiplet calculations (e) with the `CTM4XAS` program are also shown for comparison. They are shifted to align the first main peaks of the L_3-edge to the LF + CT multiplet result by the *ab initio* CI method (c). In the CTM calculations, energy-dependent broadening factors are used. The broadening factor for the L_2-edge is larger than that for the L_3-edge. In the case of $SrTiO_3$, the results of the *ab initio* CI method and the CTM method are consistent. In the LF multiplet calculations, the branching ratio and the small shoulders located below the first main peak of the Ti L_3-edge are well reproduced in both methods. In the CT+LF multiplet calculations, the numbers of final states contributing to the Ti $L_{2,3}$ XANES are different in those two methods because of the different treatment of ligand orbitals. Nevertheless, the spectral features are almost identical. The multiplet structures at the final states are widely spread especially in the Ti L_2-edge. Small satellite peaks around 470 eV are found in both figures 4(c) and (e).

In the Ti $L_{2,3}$ XANES of $SrTiO_3$, the small and broad satellite peaks have been observed at about 6 and 11 eV higher energy than the second main peak in the L_2-edge [42]. Okada *et al* have made the charge transfer multiplet calculation for $SrTiO_3$ and have concluded that those satellite peaks can be ascribed to the ligand–metal charge transfer [43]. In the present CTM and the *ab initio* CI calculations, those satellite peaks are reproduced (not explicitly shown in figures 4(c) and (e)). However, they are shifted to higher energy by about 4 eV, which might be improved by including additional higher charge transfer channels.

In the case of Ni $L_{2,3}$ XANES of NiO, the LF multiplet results by the *ab initio* CI method and by the CTM method are significantly different. The large discrepancies between those two spectra can be ascribed to the large difference of the $(t_{2g})^6(e_g)^2$ composition at the initial states. As mentioned in section 4.4, the contribution of the $(t_{2g})^6(e_g)^2$ configuration is abnormally small in the case of the LF multiplet calculation by the *ab initio* CI method because of the large reduction of two-electron integrals from atomic values. In the case of the CTM calculation, the atomic values were adopted for the inter-electron interactions. The contribution of $(t_{2g})^6(e_g)^2$ is 99% at the initial state.

When the CT configuration is added, the characteristic features of the experimental spectrum (figure 5(a)) are reproduced by both *ab initio* CI and the CTM methods (figures 5(c) and (e)). The charge transfer satellite peaks are also reproduced by both methods. Comparing the two theoretical spectra, however, several differences can be recognized. In the case of the *ab initio* CI method, the positions of CT satellite peaks are shifted about 2 eV to higher energy compared with the CTM result and the experimental spectrum. This might be improved by properly taking the band structures of ligands in the solid state. In addition, the energy separation between the L_3 and the L_2-edges is overestimated in the *ab initio* CI method because of neglecting the relativistic effects for inter-electron interactions [20].

One can also find that the intensity ratios between the two L_2 peaks in the *ab initio* CI and CTM results are slightly different from those in the experimental spectrum. It has been shown that the Ni $L_{2,3}$ XANES of NiO is sensitive to the super-exchange interaction coupling the spins on the different Ni sites. Alders *et al* have reported the clear temperature dependence of the Ni L_2 part of XANES for 20 monolayers of NiO on MgO(100) [44]. This effect can be simulated by adding an exchange field to the ground states by including the 3d spin–orbit coupling. In the present calculations, 3d spin–orbit coupling was taken into account, but the exchange field due to the spin–spin correlations on the different Ni sites is not taken into account.

5. Alternative approaches

Other routes to the multiplet calculation of $L_{2,3}$ XANES, which explicitly treat the interaction between a core–hole and excited electron in conjunction with band structures in solids, have been reported by several groups. Zaanen *et al* developed a two-particle Green's function method which treats the fully atomic Coulomb and exchange interactions as well as the solid state band structure method [45]. The spectral shapes were affected by the 3d partial density of states. In their calculations, however, the 3d bands were always empty at the ground state. In other words, the interactions between a core–hole and the excited electron to the pre-existing 3d electrons were neglected. As mentioned in the literature, this approximation is only expected to be valid when the 3d bandwidths are much larger than the U_{3d3d} and U_{2p3d}. For systems with narrow d-bands, like ionic compounds, the interaction among 3d electrons cannot be neglected in the ground state.

The multiple scattering (MS) method based on the single-particle approximation has been applied for the calculation of $L_{2,3}$ XANES of Cu and Co metals by the group of Rehr [46]. After that, Krüger and Natoli have applied the multi-channel multiple scattering (MCMS) theory for the calculations of Ca

$L_{2,3}$ XANES for Ca metal and CaO and CaF_2 [47]. In the MCMS method, the multiplet structure of $(2p)^5(3d)^1$ final states was rigorously calculated. Similar to the DFT–CI method, the interaction with the other electrons was taken into account through the effective one-electron potential optimized for the system. The MCMS method can handle the larger cluster models including several hundred atoms, and thus can include solid state effects more accurately. This method is feasible for the calculation of TM-$L_{2,3}$ XANES for both metallic and insulating compounds. However, as yet the MCMS method is limited to systems that have an empty 3d band in the ground state.

The band structure calculation based on the Bethe–Salpeter equation (BSE) has also been applied to the TM-$L_{2,3}$ XANES of d^0 systems by Shirley [48]. The two-particle equation for the core–hole and the excited electron has been solved. The core–hole screening effects have been treated within the random phase approximation [49]. In this method, the XANES spectra have been calculated by the plane-wave-based pseudopotential and the solid state effects are *de facto* included. Similar methods based on the time-dependent DFT (TD-DFT) have been used by the groups of Ebert and Rehr [50, 51].

Compared to the CTM or the *ab initio* CI approaches, the methods discussed can treat the solid state effects more accurately. This is quite important for the $L_{2,3}$ XANES of metallic or highly covalent compounds, in which the 3d orbitals are spatially delocalized and form wide 3d bands. In those systems, more than one TM atom should be included in the models. As already mentioned in section 4.4, the *ab initio* CI calculations using the cluster models including multiple TM sites are available for few systems due to the limitation of computational power. The CTM approach cannot handle cluster models including multiple TM sites.

A big problem of these methods is that neither the multiplet structures of the strong correlation among 3d electrons nor the charge transfer effects are treated correctly. In the MCMS method, these effects can be included by taking additional channels into the CI with the expense of computational cost. In the other two methods, these effects cannot be included in a straightforward manner since they are based on the two-particle theory. In the CTM and the *ab initio* CI approach, both multiplet and CT effects are explicitly considered.

6. Outlook

In this paper, the two different methods to calculate the $L_{2,3}$ XANES for 3d transition-metal (TM) compounds are reviewed. One is the semi-empirical charge transfer multiplet (CTM) approach and the other is the relativistic configuration-interaction method in quantum chemistry which is an *ab initio* approach except for the peak broadness. In the *ab initio* CI method, the multiplet structure is described based on molecular orbitals (MOs) instead of atomic orbitals (AOs). This is the one of the largest differences between the *ab initio* CI method and the CTM approach. All ligand field effects including the crystal field and the covalent bonding between a TM ion and the ligand atoms are automatically included by using MOs. The reduction of the two-electron integrals from the atom to the solid state is found by the *ab initio* CI method. The larger the covalent bonding between the TM atom and ligands becomes, the more the two-electron integrals are reduced.

The charge transfer effects are treated as the configuration interactions among two or more electronic configurations, e.g. $3d^n + 3d^{n+1}\underline{L}$ in the CTM approach and $(\phi_{3d})^n + (\phi_{3d})^{n+1}(\phi_{O\ 2p})^{-1}$ in the *ab initio* CI method. The charge transfer multiplet structure can be calculated in an *ab initio* manner by the latter method. The contribution of the charge transfer energy Δ and the hopping parameters T used in the CTM approach are rigorously calculated using the one- and two-electron integrals over MOs. The composition of the charge-transferred configuration in the *ab initio* CI method is much smaller than that in the CTM approach at both initial and final states of TM-$L_{2,3}$ XANES. This is because a part of the charge transfer in the CTM approach is taken into account as the covalency between the TM ion and the ligand atoms which is included by using the MOs in the case of the *ab initio* CI method. Future developments should include the addition of more and other charge transfer channels, depending on the systems studied. This should include the addition of at least two metal sites, for example in a M_2O_9 or M_2O_{11} cluster. Within the present program and computer power, such calculations are not possible yet in most cases.

Acknowledgments

This work was supported by a Grant-in-Aid for Scientific Research on Priority Areas 'Nano Materials Science for Atomic Scale Modification 474' from the Ministry of Education, Culture, Sports, Science and Technology (MEXT) of Japan. ES and FMFdG acknowledge financial support by the Netherlands Organization for Scientific Research (NWO-CW) for a veni and a vici grant.

References

[1] de Groot F and Kotani A 2008 *Core Level Spectroscopy of Solids* (*Advances in Condensed Matter Science*) (Boca Raton, FL: CRC Press)

[2] de Groot F M F, Fuggle J C, Thole B T and Sawatzky G A 1990 $L_{2,3}$ x-ray-absorption edges of d^0 compounds: K^+, Ca^{2+}, Sc^{3+} and Ti^{4+} in o_h (octahedral) symmetry *Phys. Rev.* B **41** 928–37

[3] de Groot F M F, Fuggle J C, Thole B T and Sawatzky G A 1990 2p x-ray absorption of 3d transition-metal compounds: an atomic multiplet description including the crystal field *Phys. Rev.* B **42** 5459–68

[4] Martins M, Godehusen K, Richter T, Wernet P and Zimmermann P 2006 Open shells and multi-electron interactions: core level photoionization of the 3d metal atoms. *J. Phys. B: At. Mol. Opt. Phys.* **39** R79–125

[5] de Groot F 2005 Multiplet effects in x-ray spectroscopy *Coord. Chem. Rev.* **249** 31–63

[6] Zaanen J, Sawatzky G A and Allen J W 1985 Band gaps and electronic structure of transition-metal compounds *Phys. Rev. Lett.* **55** 418–21

[7] Okada K, Kawai J and Kotani A 1993 Triple-peak feature of Cu 2p x-ray-photoemission spectrum in copper acetylacetonate *Phys. Rev.* B **48** 10733–8

[8] Hocking R K, Wasinger E C, de Groot F M F, Hodgson K O, Hedman B and Solomon E I 2006 Fe L-edge XAS studies of

$K_4[Fe(Cn)_6]$ and $K_3[Fe(Cn)_6]$: a direct probe of back-bonding *J. Am. Chem. Soc.* **128** 10442–51
[9] Hocking R K, Wasinger E C, Yan Y-L, de Groot F M F, Walker F A, Hodgson K O, Hedman B and Solomon E I 2007 Fe L-edge x-ray absorption spectroscopy of low-spin heme relative to non-heme Fe complexes: Delocalization of Fe d-electrons into the porphyrin ligand *J. Am. Chem. Soc.* **129** 113–25
[10] Wasinger E C, de Groot F M F, Hedman B, Hodgson K O and Solomon E I 2003 L-edge x-ray absorption spectroscopy of non-heme iron sites: experimental determination of differential orbital covalency *J. Am. Chem. Soc.* **125** 12894–906
[11] Ogasawara K, Iwata T, Koyama Y, Ishii T, Tanaka I and Adachi H 2001 Relativistic cluster calculation of ligand-field multiplet effects on cation $L_{2,3}$ x-ray-absorption edges of $SrTiO_3$, NiO, and CaF_2 *Phys. Rev.* B **64** 115413
[12] Ikeno H, Mizoguchi T, Koyama Y, Kumagai Yu and Tanaka I 2006 First-principles multi-electron calculations for $L_{2,3}$ ELNES/XANES of 3d transition metal monoxides *Ultramicroscopy* **106** 970–5
[13] Ikeno H, Tanaka I, Koyama Y, Mizoguchi T and Ogasawara K 2005 First-principles multielectron calculations of Ni $L_{2,3}$ NEXAFS and ELNES for $LiNiO_2$ and related compounds *Phys. Rev.* B **72** 075123
[14] Dirac P A M 1981 *The Principles of Quantum Mechanics* (*The International Series of Monographs on Physics*) 4th edn (New York: Oxford University Press) chapter XI (Relativistic Theory of The Electron)
[15] Bethe H A and Salpeter E E 1957 *Quantum Mechanics of One- and Two-Electron Atoms* (New York: Academic)
[16] Desclaux J-P, Thaller B, Grant I P, Quiner H M, Andrea D, Faegri H Jr, Dyall K G, Visscher L, Saue T, Labzowsky L N, Goidenko I, Sapirstein J, Engel E, Wolf A, Reiher M, Hess B A, Kutzelnigg W, Sandholm D, Dolg M and Christensen N E 2002 *Relativistic Electronic Structure Theory Part 1. Fundamentals* (*Theoretical and Computational Chemistry* vol II) 1 edn (Amsterdam: Elsevier)
[17] Sucher J 1980 Foundations of the relativistic theory of many-electron atoms *Phys. Rev.* A **22** 348–62
[18] Sucher J 1987 Relativistic many-electron Hamiltonians *Phys. Scr.* **36** 271–81
[19] Mittleman M H 1981 Theory of relativistic effects on atoms: configuration-space Hamiltonian *Phys. Rev.* A **24** 1167–75
[20] Ikeno H and Tanaka I 2008 Effects of Breit interaction on the $L_{2,3}$ x-ray absorption near-edge structures of 3d transition metals *Phys. Rev.* B **77** 075127
[21] Chen M H, Cheng K T and Johnson W R 1993 Relativistic configuration-interaction calculations of $n = 2$ triplet-states of heliumlike ions *Phys. Rev.* A **47** 3692–703
[22] Cheng K T, Chen M H, Johnson W R and Sapirstein J 1994 Relativistic configuration-interaction calculations for the ground-state and $n = 2$ singlet states of helium like ions *Phys. Rev.* A **50** 247–55
[23] Visscher L, Saue T, Nieuwpoort W C, Faegri K and Gropen O 1993 The electronic-structure of the pth molecule: Fully relativistic configuration interaction calculations of the ground and excited states *J. Chem. Phys.* **99** 6704–15
[24] Eliav E, Kaldor U and Ishikawa Y 1994 Open-shell relativistic coupled-cluster method with Dirac–Fock–Breit wavefunctions: energies of the gold atom and its cation *Phys. Rev.* A **49** 1724–9
[25] Landau A, Eliav E, Visscher L and Kaldor U 2002 Potential functions of Al_2 by the relativistic Fock-space coupled cluster method *Int. J. Mol. Sci.* **3** 498–507
[26] Marian C M, Blomberg M R A and Siegbahn P E M 1989 Multireference and relativistic effects in NiH *J. Chem. Phys.* **91** 3589–95
[27] Laerdahl J K, Fægri K, Visscher L and Saue T 1998 A fully relativistic Dirac–Hartree–Fock and second-order Moller–Plesset study of the lanthanide and actinide contraction *J. Chem. Phys.* **109** 10806–17
[28] Vilkas M J, Koc K and Ishikawa Y 1998 Relativistic multireference Møller–Plesset perturbation theory based on multiconfigurational Dirac–Fock reference functions *Chem. Phys. Lett.* **296** 68–76
[29] Rajagopal A K and Callaway J 1973 Inhomogeneous electron gas *Phys. Rev.* B **7** 1912–9
[30] MacDonald A H and Vosko S H 1979 A relativistic density functional formalism *J. Phys. C: Solid State Phys.* **12** 2977–90
[31] Engel E and Dreizler R M 1996 *Density Functional Theory II: Relativistic and Time Dependent Extensions* (*Springer Topics in Current Chemistry* vol 181) (Berlin: Springer)
[32] Ogasawara K, Ishii T, Tanaka I and Adachi H 2000 Calculation of multiplet structures of Cr^{3+} and V^{3+} in α-Al_2O_3 based on a hybrid method of density-functional theory and the configuration interaction *Phys. Rev.* B **61** 143–61
[33] Rósen A, Ellis D E, Adachi H and Averill F W 1976 Calculations of molecular ionization energies using a self-consistent-charge Hartree–Fock–Slater method *J. Chem. Phys.* **65** 3629–34
[34] Crocombette J P and Jollet F 1996 Covalency effect on cation 2p x-ray absorption spectroscopy in 3d transition-metal oxides *J. Phys.: Condens. Matter* **8** 5253–68
[35] Kumagai Y, Ikeno H, Oba F, Matsunaga K and Tanaka I 2008 Effects of crystal structure on Co-$L_{2,3}$ x-ray absorption near-edge structure and electron-energy-loss near-edge structure of trivalent cobalt oxides *Phys. Rev.* B **77** 155124
[36] Bagus P S and Ilton E S 2006 Effects of covalency on the p-shell photoemission of transition metals: MnO *Phys. Rev.* B **73** 155110
[37] Mulliken R S 1955 Electronic population analysis on LCAO-MO molecular wavefunctions. I *J. Chem. Phys.* **23** 1833–40
[38] Uehara Y, Lindle D W, Callcott T A, Terminello L T, Himpsel F J, Ederer D L, Underwood J H, Gullikson E M and Perera R C C 1997 Resonant inelastic scattering at the L edge of Ti in barium strontium titanate by soft x-ray fluorescence spectroscopy *Appl. Phys.* A **65** 179–82
[39] Gilbert B, Frazer B H, Belz A, Conrad P G, Nealson K H, Haskel D, Lang J C, Srajer G and De Stasio G 2003 Multiple scattering calculations of bonding and x-ray absorption spectroscopy of manganese oxides *J. Phys. Chem.* A **107** 2839–47
[40] Regan T J, Ohldag H, Stamm C, Nolting F, Lüning J, Stöhr J and White R L 2001 Chemical effects at metal/oxide interfaces studied by x-ray-absorption spectroscopy *Phys. Rev.* B **64** 214422
[41] van der Laan G, Zaanen J, Sawatzky G A, Karnatak R and Esteva J M 1986 Comparison of x-ray absorption with x-ray photoemission of nickel dihalides and NiO *Phys. Rev.* B **33** 4253–63
[42] van der Laan G 1990 Polaronic satellites in x-ray-absorption spectra *Phys. Rev.* B **41** 12366–8
[43] Okada K, Uozumi T and Kotani A 1993 Charge-transfer satellites in Ti 2p XAS and XPS of Ti compounds *Japan. J. Appl. Phys.* 1 **32** 113–5
[44] Alders D, Tjeng L H, Voogt F C, Hibma T, Sawatzky G A, Chen C T, Vogel J, Sacchi M and Iacobucci S 1998 Temperature and thickness dependence of magnetic moments in NiO epitaxial films *Phys. Rev.* B **57** 11623–31
[45] Zaanen J, Sawatzky G A, Fink J, Speier W and Fuggle J C 1985 $L_{2,3}$ absorption spectra of the lighter 3d transition metals *Phys. Rev.* B **32** 4905–13
[46] Nesvizhskii A I and Rehr J J 1999 L-edge XANES of 3d-transition metals *J. Synchrotron Radiat.* **6** 315–6
[47] Krüger P and Natoli C R 2004 X-ray absorption spectra at the Ca $L_{2,3}$ edge calculated within multichannel multiple scattering theory *Phys. Rev.* B **70** 245120

[48] Shirley E L 2005 Bethe–Salpeter treatment of x-ray absorption including core–hole multiplet effects *J. Electron Spectrosc. Relat. Phenom.* **144–147** 1187–90

[49] Soininen J A and Shirley E L 2001 Scheme to calculate core hole–electron interactions in solids *Phys. Rev.* B **64** 165112

[50] Schwitalla J and Ebert H 1998 Electron core–hole interaction in the x-ray absorption spectroscopy of 3d transition metals *Phys. Rev. Lett.* **80** 4586–9

[51] Ankudinov A L, Nesvizhskii A I and Rehr J J 2003 Dynamic screening effects in x-ray absorption spectra *Phys. Rev.* B **67** 115120